UPPSALA
UNIVERSITET

Digital Comprehensive Summaries of Uppsala Dissertations from the Faculty of Science and Technology **994**

Multiphase Contamination in Rock Fractures

Fluid Displacement and Interphase Mass Transfer

ZHIBING YANG

ACTA
UNIVERSITATIS
UPSALIENSIS
UPPSALA
2012

ISSN 1651-6214
ISBN 978-91-554-8531-3
urn:nbn:se:uu:diva-183720

Dissertation presented at Uppsala University to be publicly examined in Hambergsalen, Geocentrum, Villavägen 16, Uppsala, Friday, December 14, 2012 at 10:00 for the degree of Doctor of Philosophy. The examination will be conducted in English.

Abstract
Yang, Z. 2012. Multiphase Contamination in Rock Fractures: Fluid Displacement and Interphase Mass Transfer. Acta Universitatis Upsaliensis. *Digital Comprehensive Summaries of Uppsala Dissertations from the Faculty of Science and Technology* 994. 75 pp. Uppsala. ISBN 978-91-554-8531-3.

Multiphase flow and transport in fractured rock is of importance to many practical and engineering applications. In the field of groundwater hydrology an issue of significant environmental concern is the release of dense non-aqueous phase liquids (DNAPLs) which can cause long-term groundwater contamination in fractured aquifers. This study deals with two fundamental processes – fluid displacement and interphase mass transfer – concerning the behavior of the multiphase contaminants in fractured media. The focus of this work has been placed on improving the current understanding of small-scale (single fracture) physics by a combined effort of numerical modeling analysis, laboratory experiments and model development. This thesis contributes to the improved understanding through several aspects. Firstly, the effect of aperture variability, as characterized by geostatistical parameters such as standard deviation and correlation length, on the DNAPL entrapment, dissolution and source-depletion behaviors in single fractures was revealed. Secondly, a novel, generalized approach (adaptive circle fitting approach) to account for the effect of in-plane curvature of fluid-fluid interfaces on immiscible fluid displacement was developed; the new approach has demonstrated good performance when applied to simulate previously published experimental data. Thirdly, the performance of a continuum-based two-phase flow model and an invasion percolation model was compared for modeling fluid displacement in a variable-aperture fracture and the dependence of fracture-scale capillary pressure – saturation relationships on aperture variability was studied. Lastly, through experimental studies and mechanistic numerical modeling of DNAPL dissolution, kinetic mass transfer characteristics of two different entrapment configurations (residual blobs and dead-end pools) were investigated. The obtained understanding from this thesis will be useful for predictive modeling of multiphase contaminant behavior at a larger (fracture network) scale.

Keywords: multiphase flow; dissolution; mass transfer; invasion percolation; immiscible displacement; fractured media; groundwater contamination; non-aqueous phase liquid; curvature

Zhibing Yang, Uppsala University, Department of Earth Sciences, LUVAL, Villav. 16, SE-752 36 Uppsala, Sweden.

ISSN 1651-6214
ISBN 978-91-554-8531-3
urn:nbn:se:uu:diva-183720 (http://urn.kb.se/resolve?urn=urn:nbn:se:uu:diva-183720)

Akademisk avhandling som för avläggande av teknologie doktorsexamen i hydrologi vid Uppsala universitet kommer offentligen försvaras i Hambergsalen, Geocentrum, Villavägen 16, Uppsala, fredagen den 14 december, 2012, kl. 10.00. Disputationen sker på engelska.

Referat

Yang, Z. 2012. Flerfasföroreningar i sprickigt berg: Utbredning och massöverföring mellan faser. Acta Universitatis Upsaliensis. *Digital Comprehensive Summaries of Uppsala Dissertations from the Faculty of Science and Technology* 994. 75 pp. Uppsala.
ISBN 978-91-554-8531-3.

Flerfasflöde och ämnestransport i sprickigt berg är av betydelse för många praktiska och tekniska problem. Tunga, svårlösliga organiska vätskor (engelska: dense non-aqueous phase liquids: DNAPLs; t.ex. klorerade lösningsmedel) kan orsaka långvarig förorening av vattenresurser, inklusive akviferer i sprickigt berg, och utgör ett viktigt miljöproblem inom grundvattenhydrologin. Denna studie behandlar två fundamentala processer för spridning av flerfasföroreningar i sprickiga medier – utbredning av den organiska vätskan och massöverföring mellan organisk vätska och vatten. Arbetet har fokuserat på att förbättra nuvarande kunskap om de fysikaliska processerna på liten skala (enskilda sprickor) genom en kombination av numerisk modellering, laboratorieexperiment och modellutveckling. Avhandlingen har bidragit till utökad processförståelse i flera avseenden. För det första har arbetet belyst effekterna av sprickaperturens variabilitet, uttryckt med geostatistiska parametrar som standardavvikelse och rumslig korrelationslängd, på fastläggning och lösning av organiska vätskor i enskilda sprickor, samt utmattningsbeteendet hos dessa källor till grundvattenförorening. För det andra har en ny, generell metod (adaptiva cirkelpassningsmetoden) för att ta hänsyn till effekten av krökningen av gränsytan mellan organisk vätska och vatten i sprickplanet utvecklats; denna metod har visats fungera väl i simuleringar av tidigare publicerade experimentella data. För det tredje, har en jämförelse gjorts mellan en kontinuumbaserad tvåfasflödesmodell och en invasions-perkolationsmodell med avseende på hur väl de kan simulera tvåfasflöde i en spricka med varierande apertur. Här studerades även hur relationen mellan kapillärtryck och mättnadsgrad på sprickplansskala beror av variabiliteten i sprickapertur. Till sist undersöktes lösning av den organiska vätskan i grundvatten för två fastläggningsscenarier (fastläggning i immobila droppar och ansamling i fällor – ”återvändssprickor”) både genom experiment och mekanistisk numerisk modellering. Kunskapen som tagits fram i denna avhandling bedöms vara användbar även för att modellera spridningen av flerfasföroreningar på större (spricknätverks-) skalor.

Nyckelord: flerfasflöde; lösning; massöverföring; invasion perkolation; sprickigt berg; grundvattenförorening; flerfasföroreningar; gränsytans krökning

Zhibing Yang, Uppsala University, Department of Earth Sciences, LUVAL, Villav. 16, SE-752 36 Uppsala, Sweden.

ISSN 1651-6214
ISBN 978-91-554-8531-3
urn:nbn:se:uu:diva-183720 (http://urn.kb.se/resolve?urn=urn:nbn:se:uu:diva-183720)

List of Papers

This thesis is based on the following papers, which are referred to in the text by their Roman numerals.

I Yang, Z., Niemi, A., Fagerlund, F., Illangasekare, T.H. (2012) Effect of single-fracture aperture statistics on entrapment, dissolution and source depletion behavior of dense non-aqueous phase liquids. *Journal of Contaminant Hydrology, 133*:1-16. Copyright 2012 Elsevier.

II Yang, Z., Niemi, A., Fagerlund, F., Illangasekare, T.H. (2012) A generalized approach for estimation of in-plane curvature in invasion percolation models for drainage in fractures. *Water Resources Research*, 48, W09507. Copyright 2012 American Geophysical Union.

III Yang, Z., Niemi, A., Fagerlund, F., Illangasekare, T.H. (2012) Two-phase flow in rough-walled fractures: Comparison of continuum and invasion-percolation models. Accepted with moderate revisions. *Water Resources Research*.

IV Yang, Z., Niemi, A., Fagerlund, F., Illangasekare, T.H., Detwiler, R. (2012) Dissolution of dense non-aqueous phase liquids in vertical fractures: Effect of finger residuals and dead-end pools. Submitted to *Journal of Contaminant Hydrology*.

Reprints were made with permission from the respective publishers.

In all the above listed papers, I was responsible for development of conceptual and numerical models, experimental design and equipment setup, running and monitoring of experiments, numerical modeling, analysis and interpretation of results and writing of the papers. Other co-authors contributed with advice and feedback on the research work involved in these papers and writing of the papers.

In addition, I have contributed to the following papers, related to the thesis but not appended to it.

Yang, Z., Zandin, H., Niemi, A., Fagerlund, F. (2012) The role of geological heterogeneity and variability in water infiltration on non-aqueous phase liquid migration. *Environmental Earth Sciences*, doi:10.1007/s12665-012-1894-6 (In Press)

Yang, Z., Tian, L., Niemi, A., Fagerlund, F. (2012) Upscaling of the constitutive relationships for CO2 migration in multi-modal heterogeneous formations. *International Journal of Greenhouse Gas Control*, under revision.

Tong, F., Niemi, A., Yang, Z., Fagerlund, F., Licha, T., Sauter, M. (2012) A numerical model of tracer transport in a non-isothermal two-phase flow system for CO2 geological storage characterization. *Transport in Porous Media*, under revision.

Contents

Abbreviations

1D	One-dimensional
2D	Two-dimensional
3D	Three-dimensional
BC	Brooks-Corey (capillary pressure function)
ACF	Adaptive circle fitting approach
AE	Average error
CCD	Charge-coupled device
CPV	Cumulative pore volumes
DNAPL	Dense non-aqueous phase liquid
IP	Invasion percolation
ISCO	*In situ* chemical oxidation
LNAPL	Light non-aqueous phase liquid
MP	Matching percentage
NAE	Normalized average error
NAPL	Non-aqueous phase liquid
NIC	Neglecting in-plane curvature
PCE	Tetrachloroethene
T2VOC	TOUGH2 module for volatile organic compounds
TCE	Trichloroethene
TOUGH2	Transport Of Unsaturated Groundwater and Heat - an numerical simulation code
VG	van Genuchten (capillary pressure function)

Introduction

Organic liquid contamination in the subsurface

Organic liquids such as petroleum fuels, chlorinated solvents and coal tars are frequently encountered contaminants of the subsurface environment. Sources of these liquids include leakage in underground storage tanks and pipes, accidental surface spills and improper disposal practices (Abriola and Bradford, 1998). Commonly known as non-aqueous phase liquids (NAPLs), most of these organic liquids are only scarcely soluble (immiscible) in water, yet producing dissolved pollutant concentrations several orders of magnitude higher than the drinking water limits or regulatory standards and thus can serve as long-term soil and groundwater contamination sources (Mackay and Cherry, 1989). Our understanding of the physical and chemical behaviors of NAPLs in the subsurface is critical for reliable risk assessment and design of effective remediation or preventive strategies. There has been extensive experimental and numerical effort endeavored to this understanding due to the widespread issues of groundwater contamination by NAPLs (see reviews by e.g., Mercer and Cohen, 1990; Khachikian and Harmon, 2000; Oostrom et al., 2006, 2007).

Once released into the subsurface, a NAPL migrates as a separate phase and partitions into the groundwater and/or the soil air. Light non-aqueous phase liquids (LNAPLs) have lower densities than water and tend to form a layer on the top of the water table. They include gasoline, jet fuel and most non-halogenated petroleum products and are often a mixture of many chemical compounds. Dense non-aqueous phase liquids (DNAPLs) have larger densities than water and thus can penetrate the water table and continue downward migration in the saturated zone. Chlorinated solvents such as trichloroethene (TCE) and tetrachloroethene (PCE) form a class of DNAPL compounds that have been widely used in industry (Kueper et al., 2003). Typical industrial processes involving these chemicals include dry cleaning, metal degreasing, chemical intermediates, pesticide formulation, and so on. A detailed review on properties, models and characterization of NAPLs in the subsurface can be found in Mercer and Cohen (1990).

Fate and transport of NAPLs in the subsurface depend not only on the NAPL properties and the release conditions but also on the properties of the geological media. The ever-present heterogeneity in subsurface-medium properties at different scales makes predictive modeling an intricate prob-

lem. Two types of media – granular media and fractured media – are typically distinguished for modeling flow and transport in the subsurface. In this thesis the focus has been placed on studying NAPL transport in the latter – fractured media.

Fractured subsurface media

Fractures are mechanical breaks (discontinuities) in rocks. They form in response to lithostatic, tectonic, and thermal stresses and high fluid pressures, occurring at different scales, from microscopic to continental (National Research Council or NRC, 1996). As conduits for fluid flow, fractures are studied in a number of contexts, including engineering construction, petroleum recovery, geotechnics and hydrogeology. While multiphase flow phenomena in porous media has received much attention and been studied for many decades, multiphase flow in fractured media has been understood to a less extent. Model development both for the general understanding of multiphase flow in fractured media and for specific applications is in great need.

An important scenario involving multiphase flow in fractured media is organic liquid contamination in fracture aquifers. DNAPLs released into the subsurface can migrate rapidly through unconsolidated sediments and reach fractured bedrocks or clay aquitards. In many places, such as in large parts of Scandinavia, fractured rocks are also exposed at or near the land surface, thereby being even more vulnerable to pollution by the organic liquids. Depending on the fracture apertures, pooling may occur before sufficient pressure buildup occurs for the DNAPLs to overcome capillary resistance and enter the fracture. Having infiltrated to fractures and fracture networks, DNAPLs will migrate under the influence of gravitational, viscous, and capillary forces until they get trapped in dead-end fractures or as immobilized residual blobs along the migration pathways. Because of the relatively little void space and small retention capacity of fractures, even a small release of DNAPL can lead to extensive spreading of the non-aqueous contaminant phase (Mackay and Cherry, 1989). Entrapped DNAPLs will act as long-term contamination sources as they dissolve into the surrounding aqueous phase and diffuse into the rock matrix through the fracture walls.

The complex heterogeneity of fracture networks and the nature of multiphase flow make it exceptionally difficult to accurately predict or characterize the spatial location and distribution of DNAPL. Technological limitations and impracticality resulting from fractured rocks introduce large uncertainty in site characterization and often prohibit successful remediation or source-zone depletion. A NRC (2005) report has identified DNAPL-contaminated fractured sites as the most difficult category of sites to remediate and manage. How a DNAPL infiltrates and becomes entrapped within a single fracture of a network determines the subsequent dissolution of the

entrapped DNAPL and its longevity. Predicting the dissolved contaminant mass flux generation from entrapped DNAPLs requires understanding of both the DNAPL entrapment and its dissolution kinetics.

Objectives and aims

The overall aim of this thesis was to develop methods and models to describe fluid displacement and entrapment as well as interphase mass transfer processes in rock fractures. This was addressed by combined efforts of numerical simulation analyses, model developments as well as experimental studies, with special emphasis on the problem of groundwater contamination by organic liquids.

The specific objectives of this study were:

i. to investigate the effect of aperture field geostatistical parameters on the DNAPL entrapment, dissolution and source-depletion behaviors in a single fracture (Paper **I**);
ii. to develop an innovative, generalized approach to account for the effect of in-plane curvature on immiscible fluid displacement (Paper **II**);
iii. to compare the performance of a continuum-based model and an invasion percolation (IP) model for describing fluid invasion processes and to develop fracture-scale capillary pressure – saturation relationships for different aperture field heterogeneity parameters (Paper **III**); and
iv. to develop a computational model for DNAPL dissolution in variable-aperture fractures and to quantify the effect of residual blobs and dead-end pools through constitutive relationships of the dissolved mass flux generation (Paper **IV**).

In the remaining text, recent advances in the topic of multiphase flow and transport in fractures are presented followed by models developed in this study, experimental work, results and conclusions.

Multiphase flow and transport in fractures

A number of important natural processes and engineering applications, including unsaturated flow in the vadose zone, groundwater contamination by immiscible fluids and its remediation, nuclear waste storage in the deep underground, geological storage of CO_2, oil/gas recovery and geothermal exploitation, can involve flow of more than one fluid phase in fractured geological formations. Flow and transport in fractured media has been considered to be a challenging topic to study (NRC, 1996; Berkowitz, 2002; Neuman, 2005; Sahimi, 2011) because of the complex heterogeneity and related scaling issues. Multiphase characteristics and interactions add further complication for understanding and modeling of the flow and transport processes.

In this chapter, the focus is placed on relevant processes within individual fractures which form the fundamental components of a fracture network. Although the processes in the following are mainly discussed in the context of subsurface hydrology (as in the example application of groundwater contamination by NAPLs), it is expected that some of the models and understanding developed can be directly extended to or have implications for other applications as well.

Aperture variability within a fracture

Aperture is one of the most important properties of a single fracture. However, natural fractures are typically rough-walled and have variable apertures (Brown, 1995; Hakami and Larsson, 1996). Many laboratory (e.g., Raven and Gale, 1985; Keller et al., 1995) and field studies (e.g., Rasmuson and Neretnieks, 1986; Raven et al., 1988; Novakowski et al., 1995) suggest that the representation of a rock fracture as a pair of smooth, parallel plates is inadequate for the description flow and transport. Aperture variability plays an important role in controlling fluid flow and solute transport in single fractures.

Considerable effort has been made in characterizing geostatistical properties of aperture distribution in single fractures (e.g., Brown et al., 1986; Gale, 1987; Keller, 1998). Studies by e.g., Gale (1987) and Keller (1998) used log-normal distribution to represent the measured aperture distribution, while studies by Brown (1995) and Lapcevic et al. (1999) used normal distribution

based on their measurements. These characterization studies for different rocks under different conditions may suggest some dependence of the aperture distribution on the nature of the rock and its deformation mode. With a higher normal stress that brings the surfaces into closer contact, the apertures are shifted toward lower values (Sahimi, 2011) and thus exhibiting more skewed distributions that may be fitted by log-normal or gamma distributions. More discussion on this can be found in Oron and Berkowitz (1998).

Geostatistical parameters (e.g., standard deviation, correlation length, anisotropy ratio) quantifying the aperture distribution have been proven useful to understand the effect of variable apertures on flow and transport in single fractures (Keller et al., 1999; Lee et al., 2003). However, the effect of these parameters on multiphase flow and transport with interphase mass transfer is not fully understood. Paper **I** attempts to address this topic and to provide improved understanding from a parametric sensitivity study.

Immiscible displacement

The physical nature of multiphase flow in porous or fractured media is a 'competition' between the fluids for the pore or fracture void space under the combined influence of capillary, gravitational, viscous and inertial forces. A fundamental process for the multiphase flow phenomenon is the displacement of one fluid by another immiscible one. Immiscible displacement results in a fluid phase distribution and fluid-fluid interfaces which play a critical role in the interphase mass transfer process. There has been a large body of work devoted to the study of immiscible displacement process in variable-aperture fractures. Findings from the previous studies have improved our understanding of fluid behavior in fractured media.

Experimental studies of immiscible flow in natural or artificial rough-walled fractures have provided useful insight on fracture multiphase flow properties. Persoff and Pruess (1995) visualized two-phase flow in transparent fracture replicas and the measured relative permeabilities suggest strong phase interference, with relative permeabilities reduced to very small values at intermediate saturations for both the wetting and non-wetting phases. A study of oil-water displacement in a natural limestone fracture by Reitsma and Kueper (1994) lead to the conclusion that the capillary pressure curves can be well represented by a Brooks-Corey porous-media type capillary pressure function. Chen and Horne (2006) proposed a channel tortuosity approach to describe relative permeability behavior in rough-walled fractures based on experimental observations of two-phase flow structures. A recent study of air-water two-phase flow by Nowamooz et al. (2009) showed that the generalization of the full cubic law can describe the liquid and gas relative permeabilities in the non-Darcian regime with a good accuracy. In laboratory experiments with vertical fractures (e.g., Su et al., 2004; Nicholl

and Glass, 2005), fingering has been observed for gravitationally unstable displacement. Loggia et al. (2009) showed that under the influence of buoyancy two-phase flow regimes range from tortuous fingers and random clusters to piston-like displacement with trapping, depending on different combinations of Bond numbers (representing the relative influence of gravity to capillary forces) and capillary numbers (representing the relative influence of viscous forces to capillary forces).

Variable apertures result in different influences of capillary, gravitational, and viscous forces, which control the immiscible two-phase flow (Glass et al., 2001). Several types of models have been proposed to simulate immiscible displacement in single fractures. These models include: invasion percolation (IP) models (e.g., Pyrak-Nolte et al., 1992; Meakin et al., 1992; Glass et al., 1998; Petchsingto and Karpyn, 2010; Ferer et al., 2011), continuum-based models (e.g., Murphy and Thomson, 1993) and pore network models (e.g., Hughes and Blunt, 2001; Karpyn and Piri, 2007; Piri and Karpyn, 2007; Ferer et al., 2011). In order for the pore network models to mimic the flow in the fracture, usually modifications have to be made so that the pores and the throats are treated exactly the same (Karpyn and Piri, 2007), which makes the pore network models conceptually similar to a site-IP model.

Capillary forces in a rough-walled fracture depend on the interfacial tension between the wetting and non-wetting fluids and the curvature of the fluid-fluid interface. The curvature can be represented by two principal components, one in the direction perpendicular to the fracture plane (describing the aperture-induced curvature) and one parallel to the fracture plane, describing the in-plane curvature. The larger one of the two curvatures will dominate the effect of interface curvature on capillary pressure. Therefore, if the in-plane curvature is much smaller in comparison to the aperture-induced curvature, the former can be neglected. Most conventional IP models assume that the effect of in-plane curvature can be ignored.

Generally, quasi-static phase displacement in a fracture is controlled by the competition between aperture variability which tends to roughen the interface and in-plane curvature which tends to smooth it (Glass et al., 2003). The relative influence of smoothing and roughening effect has been shown by Glass et al. (2003) to be controlled by a single parameter N_c/δ where N_c is a dimensionless curvature number which weighs the relative importance of local in-plane curvature and aperture-induced curvature and δ is the coefficient of variation of the aperture field.

A few approaches to account for the in-plane curvature have been presented in the literature. Glass (1993) and Hughes and Blunt (2001) considered three local configurations for the interface to calculate the in-plane radius. The three possible configurations were ‘flat front’, ‘two adjacent sites filled’ and ‘three adjacent sites filled’. However, this local approach allowing only three possible interface configurations often yields grid-dominated, blocky fronts. Glass et al. (1998) were the first to formulate a modified inva-

sion percolation model to include the local in-plane curvature and systematically study its influence on the displacement process. The procedure of accounting for the in-plane curvature involved tracing a selected number of nearby sites along the interface. This approach of Glass et al. (1998) requires pre-defining a typical length scale for the in-plane curvature radius. The authors related the predefined length scale to the correlation length of the aperture field. However, based on experimental data, Neuweiler et al. (2004) found that a representative length scale can be very similar for two aperture fields with distinctly different spatial correlation structures (one generated from Gaussian variogram with a finite correlation length and one with power-law variogram for which no finite correlation length). The observations lead Neuweiler et al. (2004) to relate the length scale of the in-plane curvature to factors like the mean aperture, the variance and the in-plane fluctuation of apertures. Therefore, in a rough fracture the fluid-fluid interface can be expected to show in-plane curvatures of different length scales depending on the variability of those factors.

Invasion percolation models can be modified to include gravity forces. Gravity acting on the density difference between the two fluids will either stabilize or destabilize the fluid–fluid displacement process (Meakin et al., 1992). Under these conditions, capillary forces are dominant on short length scales and the effects of gravity acting on the density difference are dominant on long length scales (Meakin et al., 2000). Modification to an IP model to include the snap-off and redistribution events in the non-wetting phase clusters was done by Amundsen et al. (1999). Invasion percolation with first order approximation to viscous forces was studied by Xu et al. (1998). When the viscosity ratio, defined as the ratio of the viscosity of the non-wetting phase to that of the wetting phase, is sufficiently small, the displacement of the wetting phase can be modeled by a form of gradient percolation under a stabilizing gradient (see e.g., Chaouche et al., 1994), similar to the case of displacement of lighter fluid from the bottom where gravity acts to stabilize the front. In the opposite case, the displacement is described by gradient percolation in a destabilized gradient and leads to capillary-viscous fingering similar to gravity-driven fingering.

In this thesis, the study of immiscible displacement in fractures focuses on model development for accounting for the effect of in-plane curvature (Paper **II**) as well as model comparison between the invasion percolation approach and the continuum-based approach (Paper **III**). The continuum-based approach is previously much less applied to fracture level modeling studies, even though it inherently accounts for detailed viscous pressure losses and thus is better suitable to the high-capillary number flow regime. This is as the continuum approach requires modifications to the general two-phase flow model in terms of representation of capillary pressure. Such development is introduced in Paper **III** and subsequently the two approaches are compared.

Interphase mass transfer

Mass transfer between two immiscible fluids is a relevant process for situations such as DNAPL dissolution into groundwater and supercritical CO_2 dissolution into residing brine of deep saline formations. For the case of DNAPL contamination in an aquifer of fractured formation, it is of particular interest for environmental practitioners and decision makers to evaluate the long term risk due to DNAPL dissolution. As discussed previously, fluid displacement and entrapment within a fracture is largely controlled by different influences of capillary, gravitational, and viscous forces as a result of the variable apertures. DNAPL entrapment structures determine the DNAPL-water interfacial area which is a key parameter for predicting interphase mass transfer. Based on DNAPL dissolution experiments in natural fractures, Dickson and Thomson (2003) developed a Sherwood-type empirical mass transfer correlation for the dissolution behavior at the fracture scale. They presented a morphology index which was used to represent the DNAPL-water interfacial area. However, the actual DNAPL entrapment morphology was not observed in the experiments. Schaefer et al. (2009) performed DNAPL dissolution experiments for four sandstone fractures and measured the interfacial area by using an interfacial tracer. The study confirmed that the dissolution rates in rock fractures were substantially smaller than those measured in unconsolidated porous media. Detwiler et al. (2001) developed a DNAPL dissolution model that explicitly incorporates the pore scale geometry of the entrapped DNAPL and its evolution during dissolution. The model demonstrated excellent agreement with comparison to high-resolution DNAPL dissolution experiments in an analog variable-aperture fracture observed by using light transmission techniques. In a later study, Detwiler et al. (2009) investigated the influence of initial entrapped phase geometry and flowing phase velocity on the dissolution processes, and developed fracture-scale constitutive relationships describing dependences of interfacial area on entrapped phase saturation, and intrinsic mass transfer rate on Peclet number.

Besides being trapped by capillary forces due to aperture variability within the fracture plane, DNAPLs can also be held stagnant due to fracture termination and/or loss of hydraulic connectivity to other fractures. Occurrences of vertical dead-end fractures can provide regions of a fractured network that accept DNAPLs due to density effects, yet do not contribute to the global flow within the network (Reynolds and Kueper, 2003). Depending on the fracture network characteristics, the volume of DNAPL entrapped in the dead-end fractures can be large. Experimental studies by e.g. Ji et al. (2003) and Su and Javandel (2004) have investigated the physical mechanisms regarding the migration of DNAPL into dead-end fractures by using laboratorial analog fractures and simple networks. Remediation of entrapped contaminants in dead-end fractures will be extremely challenging due to the

difficulty of successful delivery of a remediating agent to these regions (Yeo et al. 2003). Dissolution of DNAPL in dead-end fractures is expected to be significantly slower than that in the backbone-fracture planes, since there is limited contact between the DNAPL and the flowing water due to water bypassing. In a DNAPL-contaminated fractured aquifer, a likely scenario is that the trapped residual blobs have already dissolved while the DNAPL trapped in dead-end fractures keeps generating mass flux at low concentrations. This was shown by VanderKwaak and Sudicky (1996) who performed numerical simulations for a case of TCE dissolution in a fracture network with low porosity granite matrix.

Entrapment as residual blobs along gravity fingers and accumulation as pools in dead-end fractures are two relevant and important DNAPL retention mechanisms in a fracture network. Although the aforementioned experimental and numerical studies have provided improved understanding on DNAPL dissolution in fractured media, they have not considered the case of dissolution of residual blobs resulting from DNAPL fingers. In addition, to the best of our knowledge, detailed quantitative analysis of dissolution kinetics of entrapped DNAPLs in dead-end fractures and its implication for field-scale contaminant mass flux have not been reported in the literature. In Paper **IV**, a study combining physical experiments and mechanistic numerical modeling is presented to investigate the dissolution of DNAPL under thesis two entrapment scenarios – residual blobs and dead-end pools.

Matrix diffusion and reactive transport

The interphase mass transfer process discussed above only involves the dissolved mass flux within the fractures and thus is limited to fractured systems with negligible matrix porosity/permeability. For systems with significant matrix porosity/permeability such as fractured clays or fractured sedimentary rocks, interphase mass transfer will also occur across the interfaces at rock wall surfaces, driven by matrix diffusion – a process whereby dissolved solutes in groundwater diffuse into the rock matrix. A number of studies (e.g., Falta, 2005; Lipson et al., 2005; Parker et al., 1997) suggest that matrix diffusion accounts for a significant percentage of the contaminant mass and could be an important process for fractured porous media. In this thesis, the emphasis is put on DNAPL behavior in crystalline rocks, a typical rock type in Scandinavia. Therefore, the effect of matrix diffusion will not be further discussed.

In engineering practices, the flow and transport behavior of a multiphase system is often accompanied by chemical and/or biological processes. For instance, the remediation of chlorinated solvents in fractured rocks often involves enhanced dissolution by *in situ* chemical oxidation or ISCO (e.g., Werner and Helmke, 2003; Tunnicliffe and Thomson, 2004), or bioaug-

mented treatment (e.g., Schaefer et al., 2010). This gives rise to a multiphase multi-component reactive transport problem (Chambon et al., 2010). Another example is the long-term fate of geologically stored (and/or leaked) CO_2 which can react with the minerals of the rock matrix and may even induce geomechanical processes. Multiphase reactive transport and coupled processes are not studied in this thesis but is noted here as an important topic for future research.

Modeling

Immiscible displacement in variable aperture fractures

As mentioned in the previous chapter, immiscible displacement in fractured media is an important process for many applications. Being able to model immiscible displacement in a single variable-aperture fracture is central for our understanding of multiphase flow behavior at a larger scale where the representation of flow properties critically depends on the fluid displacement process. In the current chapter, we present two modeling approaches for modeling immiscible displacement in variable-aperture fractures, namely a continuum-based approach and an invasion percolation approach. A novel approach for accounting for the in-plane curvature is also presented.

Continuum-based approach (Paper **III**)

The fracture is conceptualized as a two-dimensional lattice with each element behaving locally like a parallel-plate fracture with an aperture $b_{i,j}$. Element volume and rectangular connection areas are assigned accordingly (see Figure 1a) and permeability $k_{i,j}$ of each location is related to aperture $b_{i,j}$, according to the cubic-law ($k_{i,j} = {b_{i,j}}^2/12$). Laminar flow in the fractures is assumed (Chen and Horne, 2006) along with a multiphase extension of Darcy's law. Assuming the fluids and the media are incompressible (e.g., in the case of NAPL-water systems), and the interphase mass transfer is negligible within the time scale of interest, we write the governing equations for immiscible two-phase flow as (Aziz and Settari, 1979; Abriola and Pinder, 1985; Keller et al., 2000):

$$\phi \frac{\partial S_\beta}{\partial t} - \nabla \cdot \left[\frac{k k_{r\beta}}{\mu_\beta} (\nabla P_\beta - \rho_\beta g \nabla z) \right] = q_\beta \tag{1}$$

where β denotes the phase ($\beta = n$ for non-wetting, $= w$ for wetting), k is the intrinsic permeability, ϕ is the porosity and is taken to be 1 here, $k_{r\beta}$ is the relative permeability of phase β, μ_β is the β-phase dynamic viscosity, P_β is the fluid pressure in phase β, q_β is the source/sink term for phase β and g is the gravitational acceleration constant, z is the position along the vertical axis. Writing equation (1) for both non-wetting and wetting phase gives us

four unknowns, S_w, P_w, S_n and P_n. Obtaining the solution of equation (1) requires using the saturation constraint ($S_w + S_n = 1$) and definition of capillary pressure P_c (the difference in pressure between wetting and non-wetting phase). It should be pointed out that applying equation (1) to a single fracture with variable apertures implicitly includes the assumption of treating the fracture like a heterogeneous two-dimensional porous medium with each pixel on the aperture field behaving like a continuum (Pruess and Tsang, 1990).

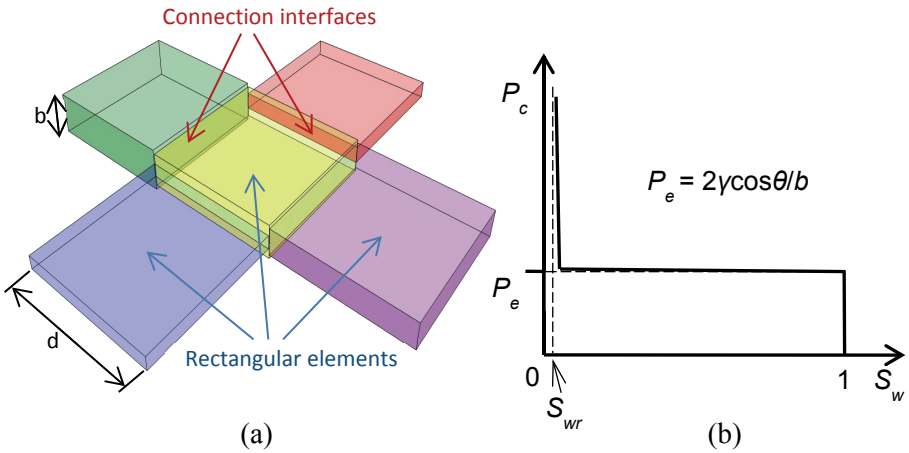

(a) (b)

Figure 1. (a) Schematic representation of numerical discretization of the rough-walled fracture. Connection area is calculated as the smaller aperture between the two elements multiplied by the resolution distance *d*. (b) Illustration of the capillary-pressure-saturation function used in the fracture-DNAPL modeling. Entry pressure P_e is defined for each element, depending on the local aperture. (Paper **I** and **III**)

While the above is common knowledge of multiphase flow, presenting the local aperture-dependent drainage is not obvious. For this, we have developed the following approach. In order to represent the process of non-wetting invasion in a wetting-phase saturated fracture, we introduce a specific capillary-pressure-saturation curve that is local to each element, as schematically shown in Figure 1b. This curve allows fast decrease of wetting phase to a residual level from a location on the fracture once the non-wetting phase entry pressure at that location is reached. The capillary pressure and more specifically the entry pressure is allowed to vary for each element according to the aperture. Non-wetting phase entry pressure P_e can be calculated using the Young-Laplace equation:

$$P_e = \gamma\left(\frac{1}{r_1} + \frac{1}{r_2}\right) \tag{2}$$

where γ is the interfacial tension, and r_1, r_2 are the principal radii of the curvature of the interface. Specifically, r_1 is the radius of the aperture-induced curvature which is dependent on local aperture value and the contact angle, and r_2 is the radius of the in-plane curvature and describes the shape of the local in-plane interface. In this continuum-based approach, we focus on cases where the effect of aperture-induced curvature dominates over that of the in-plane curvature, that is, cases with $N_c/\delta < 1$, according to the discussions by Glass et al. (2003). Therefore we have the approximation of $P_e \approx \gamma/r_1 = 2\gamma\cos\theta/b$, where θ is the contact angle and b is the aperture. Note that the effect of local convergence/divergence angles on the interface curvature is not considered here. The continuum-based approach is described in more details in Paper **III**.

The continuum-based approach is implemented into a generalized multiphase flow and transport simulator TOUGH2 (Pruess et. al., 1999) with the T2VOC (Falta et al., 1995) module. In Paper **I**, this approach is applied to simulate DNAPL migration and entrapment in vertical fractures with different geostatistics of the aperture field. In Paper **III**, a thorough comparison between the continuum model and an IP model (introduced in the following section) is presented.

Invasion percolation approach (Papers **II** and **III**)

Invasion percolation was introduced by Wilkinson and Willemsen (1983) based on the standard percolation theory (Broadbent and Hammersley, 1957) to incorporate the accessibility of fluids. In percolation-type models, quasi-static displacement is typically assumed (i.e., viscous forces are negligible with respect to capillary forces). In other words, flow rates/velocities must be small. In this approach, connected sites on a fracture plane are assigned values of invading pressure according to local apertures and phase geometries. The site that is connected to the invasion boundary or the source and has the lowest invasion pressure is found and invaded. This event modifies the list of sites connected to the invading phase, and then once again available sites are sorted and the site with the lowest pressure is invaded, and so on (Glass and Yarrington, 2003). Defending-phase trapping (meaning that the sites that become surrounded by the invading phase are removed from the available-site list) is implemented. This is done by implementing a bidirectional searching algorithm to determine whether a site or region is connected to the outlet boundary.

To model quasi-static immiscible fluid displacement in rough-walled fractures, the fracture aperture field is conceptualized as a planar checkerboard of individual aperture sites with a fourfold connectivity (same as in the continuum approach, see Figure 1a). For the sake of brevity, only drainage is described in this section. However, the main principles can be easily extended to imbibition.

The invading pressure P_{inv} for a given site is calculated as:

$$P_{inv} = \gamma(k_1 + k_2) + \Delta\rho g \Delta z \cos\varphi = \gamma\left(\frac{1}{r_1} + \frac{1}{r_2}\right) + \Delta\rho g \Delta z \cos\varphi \qquad (3)$$

where k_1, k_2 are the two principal curvatures, $\Delta\rho$ is the density difference between the two fluids ($\rho_{invader}$ - $\rho_{defender}$), Δz is the distance along the vertical axis between the potential site and the source location, and φ is the angle between the fracture plane and the gravitational vector.

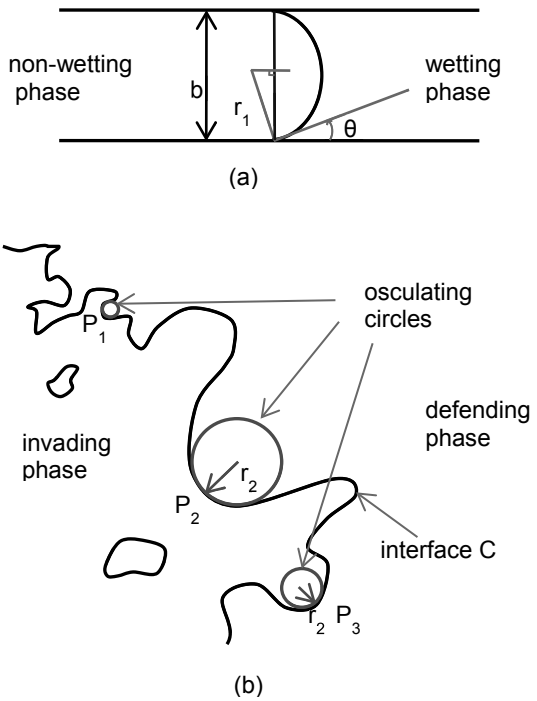

Figure 2. Illustration of two principle radii of curvature for a fluid-fluid interface within a rough-walled fracture: (a) cross section view showing the aperture-induced radius of curvature r_1 related to the local aperture b and contact angle θ; (b) fracture plane view showing the in-plane radius of curvature r_2 at point P on the interface curve C that can be determined using osculation circles. (Paper **II**)

The curvature is calculated as the reciprocal of the radius of the osculating circle. We have $k_1 = 1/r_1$, and $k_2 = 1/r_2$, where r_1, r_2 are the principal radii of curvature. We take the normal plane for the principal curvature k_1 to be perpendicular to the plane of the fracture and the normal plane for k_2 to be in the plane of the fracture. The cut between the normal plane for k_1 and the fluid-

fluid interface produces a curve that spans the fracture aperture while the cut between the normal plane for k_2 and the interface produces a curve that is within the fracture plane. Following the conventions, we refer to k_1 as aperture-induced curvature and k_2 as in-plane curvature. For the case of drainage in a rough-walled fracture, if we choose the normal at a given point or site on the fluid-fluid interface to be pointing from the interface to the inside of the non-wetting phase, then r_1 is always positive, while r_2 is then taken as positive or negative depending on whether or not the curve turns in the same direction as the chosen normal.

With the simplification of ignoring the influence of local convergence/divergence angles, r_1 can be calculated as (see Figure 2a) $r_1 = b/(2\cos\theta)$. If the in-plane curvature k_2 is much smaller than k_1 (or r_2 is much larger than r_1), the invading pressure can be approximated as $P_{inv} \approx 2\gamma\cos\theta/b + \Delta\rho g\Delta z\cos\varphi$. The invasion percolation model with this approximate P_{inv} will hereafter be referred to as the 'neglecting in-plane curvature' model or NIC model. However, in many cases, k_2 is not negligible and needs to be accounted for. In the following section a generalized approach for calculating the radius of in-plane curvature r_2 (Figure 2b) is described (Paper **II**). The performance of the above developed IP model and the extended continuum model (previous section) was compared for different invasion scenarios (Paper **III**).

Generalized approach for estimation of in-plane curvature

Aperture fields are always associated with a given measurement resolution. The modeling of immiscible displacement in these aperture fields requires discretization and adaption to the measurement resolution. This yields local fluid-fluid interfaces that are composed of discontinuous steps (not smooth). However, in reality the fluid-fluid interface is independent of grid resolution and does not have discontinuous steps. This poses the question of how to best calculate the in-plane curvature in a numerical model where the interface is composed of discontinuous steps.

In the model of Glass et al. (1998), the authors suggested the calculation of $r_2 = R\cdot\tan(\xi/2)$, where R is a pre-defined representative length scale for the in-plane curvature and ξ is the angle between two vectors from the potential invasion site to both sides of the interface. The two vectors were determined as a weighted average of unit vectors extending from the potential site to each neighboring site along the interface within a certain distance. Glass et al. (1998) proposed to use half of the correlation length of the aperture field for R. Neuweiler et al. (2004), however, treated R as a fitting parameter to match simulations and experiments and showed that the length scale R can be very similar for two aperture fields with distinctly different correlation structures. Neuweiler et al. (2004) qualitatively suggested a possible approx-

imation for R that is dependent on the mean aperture, roughness and average fluctuations of the aperture field.

Here a new approach which is adaptive to the fluid-fluid interface is proposed. This approach does not require pre-defining any global, representative length scale for the in-plane curvature. The idea is to determine the in-plane curvature by adaptively calculating the radius fitted from a circle equation using the coordinates of the neighboring interface sites to a local point. This is referred as the adaptive circle fitting (ACF) approach. Here, only the main steps are presented, the full description is presented in Paper **II**.

The ACF approach first involves fitting an osculating circle to the local fluid-fluid interface with the following steps, which are also illustrated in two examples shown in Figure 3.

(1). Identify all potential sites to be invaded (a potential site is a defending site which is next to the fluid-fluid interface and is connected to the defending boundary). Select a potential site to be invaded and choose a site (or two sites, if there exist) on the interface neighboring the potential site, from where invasion will take place.

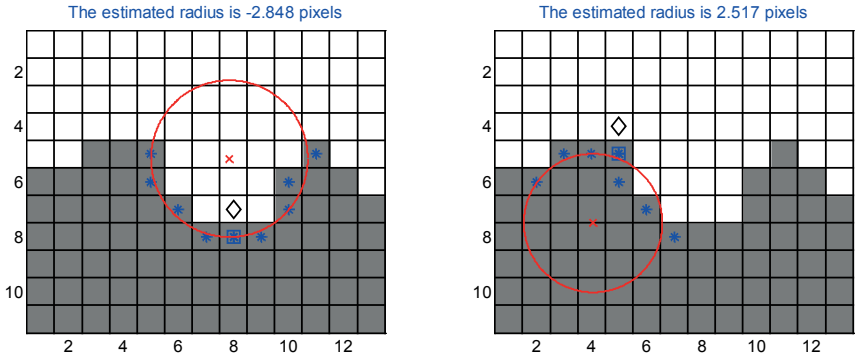

(a) (b)

Figure 3. Examples of the circle fitting approach for calculation of the in-plane curvature. Grey: invaded sites, white: uninvaded sites. The potential invasion site is marked with a diamond. The invaded interface sites which are traced to fit a circle are marked with a star. The starting interface site for tracing is marked with both a star inside a square. The cross denotes the center of the fitted circle. Picture (a) shows an example of negative curvature, the tracing number n_t = 5; Picture (b) shows an example of positive curvature, the tracing number n_t = 4. (Paper **II**)

(2). Trace a selected number (n_t) of invaded interface sites on each side of the currently considered interface site/sites, thus identifying sites at the interface that are used to determine the in-plane curvature. Tracing on both sides is done by searching both clockwise and counter-clockwise on the interface,

starting from the currently considered interface site(s). The number n_t is termed as tracing number hereafter. Note that the tracing number n_t includes the starting traced interface-site(s).

(3). Record the two-dimensional coordinates x and y (x for the column number and y for the row number in the aperture field) for the center of all the traced sites. Then fit the coordinates x and y to the equation of a circle:

$$f(x,y) = (x - x_c)^2 + (y - y_c)^2 - r^2 = 0 \tag{4}$$

where x_c, y_c and r are fitting parameters, and x_c and y_c denote the coordinates of the center of the fitted circle, and r denotes the radius of the fitted circle.

(4). Calculate the in-plane curvature k_2 as reciprocal of r and assign a positive or negative sign to k_2 according to the turning direction of the curvature with respect to the chosen normal.

It should be noted that, given a tracing number n_t, the nonlinear fitting of the coordinates of the traced interface sites to a circle always produces the fitting parameters, regardless of the goodness of the fit. Cases where some of the traced sites do not fall on or even close to the fitted circle can occur. In Figure 4a, one can see that choosing n_t = 4 gives us a better fit and n_t = 3 gives us the best fit (Figure 4b and 4c). The lower limit for n_t is 2, in which case the circle fitting approach is similar to the local-configuration approach used by e.g. Glass (1993) and Hughes and Blunt (2001).

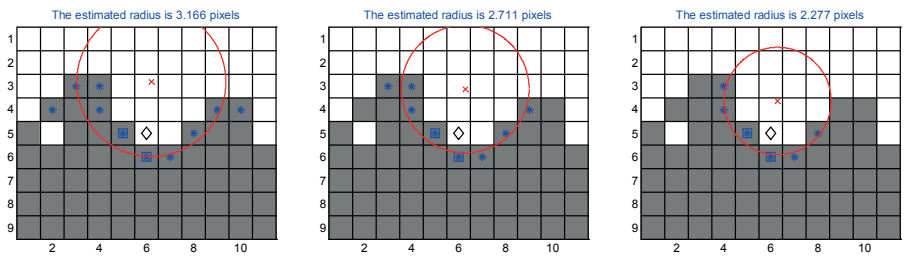

Figure 4. Circle fitting for the interface using different tracing number n_t. (a) n_t = 5, NAE = 0.156; (b) n_t = 4, NAE = 0.112; (c) n_t = 3, NAE = 0.069. (Paper **II**)

The best fitted osculating circle is adaptively determined by the use of the fitting errors as explained below.

First, the average error (AE) is calculated as follows:

$$AE = \frac{\sum_{i=1}^{N} \left| \sqrt{(x_i - x_c)^2 + (y_i - y_c)^2} - r \right|}{N} \tag{5}$$

where N is the total number of traced interface sites (N equals to 2 n_t-1 or 2 n_t), and x_i, y_i (i = 1, 2…, N) are the coordinates of the N traced sites. Graphically, AE measures the average radial distance between the circumference and the centers of the traced interface sites.

Second, AE is normalized to the fitted radius to obtain NAE (normalized average error):

$$NAE = AE / r \quad (6)$$

Third, a threshold (T) is used for the acceptance of the circle fitting results. If NAE is larger than the threshold, the fitting is declined and n_t is reduced by 1. This is repeated until NAE becomes smaller than or equal to the threshold. The threshold T means that, once the average radial distance AE falls into the interval [$-Tr$, $+Tr$] or the average distance between the centers of the traced interface sites and the circle center falls into the interval [r-Tr, r+Tr], the circle fitting is accepted. A threshold value for NAE in the range of 0.07 ~ 0.1 is recommended, based on extensive analysis of NAE for various interface configurations together with visual inspection of their corresponding circle fittings.

In Paper **II**, the ACF approach is demonstrated by simulations of drainage processes observed in previously published experiments with two fractures exhibiting different spatial correlation characteristics in the aperture fields (Neuweiler et al., 2004).

Dissolution of an entrapped fluid into water (Paper **IV**)

The mathematical equations in a full, three-dimensional (3D) form describing the dissolution of a single-component DNAPL into water in variable-aperture fracture were discussed by Detwiler et al. (2001). However, obtaining numerical solutions to these fully-coupled 3D equations is often impractical and not necessary. Using the approximation of quasi-steady state and depth-averaging for single phase flow and transport, Detwiler et al. (2001) developed a two-dimensional (2D) numerical model which could excellently reproduce their experimental results. The modeling approach used in this study is similar to that of Detwiler et al. (2001) but applied to the case of vertical fracture with gravity effects and extended to include the newly develop approach for in-plane curvature (previous section). Below, the numerical model for DNAPL dissolution and mass transport is described.

The water flow in a variable-aperture fracture is approximated by the well-known 2D Reynolds equation:

$$\nabla \cdot (b\mathbf{v}) = 0 \quad (7)$$

where b is the local aperture and the average flow velocity is given by

$$\mathbf{v} = -\frac{k\rho_w g}{\mu}\nabla h \tag{8}$$

where h is the local pressure head, k is the local permeability (calculated as $b^2/12$ according to the cubic law). ρ_w is the density of the water, μ is the viscosity of the water, g is the gravitational acceleration constant. Due to the presence of the entrapped non-aqueous phase, the fluid-fluid interface renders a zero-gradient boundary for the flowing phase.

The quasi-steady, two-dimensional equation for dissolved mass transport within a variable-aperture fracture is described by (Detwiler et al., 2001):

$$\nabla \cdot \left(b\mathbf{v}C\right) = \nabla \cdot \left(b\mathbf{D}_{\mathbf{eff}} \cdot \nabla C\right) \tag{9}$$

where C is the depth-averaged concentration and $\mathbf{D}_{\mathbf{eff}}$ is the effective dispersion tensor. According to the discussions by Detwiler et al. (2001), $\mathbf{D}_{\mathbf{eff}}$ is taken to be equal to D_m which is the molecular diffusion coefficient. The DNAPL-water interfaces impose a boundary condition as $C = C_{eq}$ where C_{eq} is the solubility (equilibrium) concentration. Local mass fluxes from the entrapped DNAPL to the flowing water are calculated as

$$j = D_m \nabla C \cdot \mathbf{n} \tag{10}$$

where $\mathbf{n}$ is the vector normal to the fluid-fluid interface. Integrating equation (10) for the local interfaces along the perimeter of each DNAPL blob gives the mass transfer fluxes for the individual blobs. It should be pointed out that by this approach the mass transfer into the wetting films is ignored and that the approach is limited to fractured rocks with negligible matrix diffusion such as crystalline rocks and shales.

Dissolution of the entrapped DNAPL into the flowing water alters the flow velocity field as more pore space becomes available for water flow. As a result, equations (7) to (10) need to be coupled. In Paper **IV**, we numerically solve these coupled equations using a centered finite difference scheme during each time step. Dissolution of the individual entrapped blobs results in shrinkage of these regions and subsequent small-scale movement of the interfaces which is controlled by interplay of capillary, gravitational and viscous forces (Detwiler et al., 2009). This interface movement process is taken into account by coupling the mass transfer results obtained from the solution of the advective-diffusive equation to a newly developed invasion percolation (IP) algorithm (Paper **II**) in which the local capillary pressure is calculated using both the aperture-induced curvature and the in-plane curvature. The computational model for DNAPL dissolution in fractures is also tested and validated against a physical experiment described in Paper **IV**.

Experiment on DNAPL dissolution

With the objective of studying the dissolution of entrapped residual blobs and testing the computational model described in the previous chapter, a physical TCE-dissolution experiment in a vertical transparent analog fracture was performed (Paper **IV**). The experiment involved three steps: (i) measurement of aperture field, (ii) TCE injection into the fracture and (iii) monitoring of entrapped TCE dissolution. A picture of the experimental system is shown below in Figure 5.

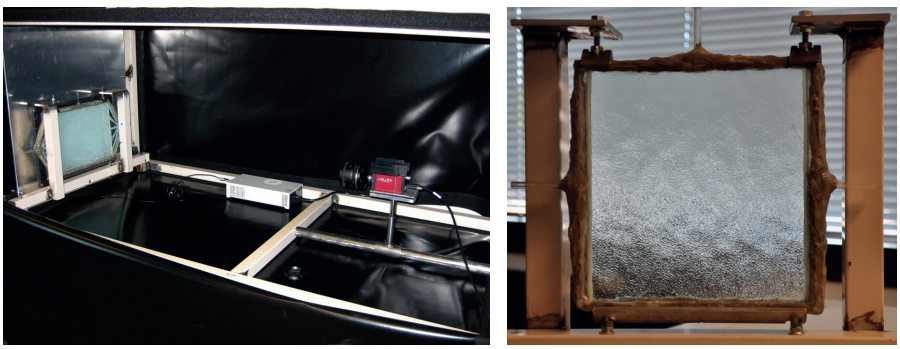

(a) (b)

Figure 5. (a) Light transmission measurement system in a dark box. (b) Transparent analog fracture cell.

Measurement of fracture apertures

A number of methods for laboratorial measurement of apertures of natural rock samples have been reported in the literature. These method include surface profiler (e.g., Brown et al., 1986), casting or injection method (e.g., Gale, 1987), nuclear magnetic resonance imaging (Dijk et al., 1999) and X-ray computed tomography (Keller, 1998). For analog fracture cells with the fracture walls made of transparent materials, light transmission techniques have been developed (Detwiler et al., 1999). The light transmission method applied to transparent analog fractures offers the advantages of accurate, non-destructive aperture measurements and convenient, continuous visuali-

zation of phase distributions in the fractures. In this work, the light transmission method was used.

The transparent analog fracture (Figure 5b) was fabricated by placing two 20 × 20 cm pieces of textured glass in contact. Each piece of glass is 8 mm thick. The four edges were sealed with cement and then covered with a layer of silicone. Prior to sealing, three fluid ports were attached to three of the edges. The port attached to top edge was used for injection of TCE and were capped during the dissolution process. The fracture cell was held vertical and water was allowed to flow from the left hand side to the right hand side. In order to distribute the inflow water evenly along the left-side boundary, a half-cylinder-shaped groove was etched on each fracture wall close to the left edge, which created an inner hollow cylinder of 6 mm diameter. This was also done for the outflow boundary.

A light transmission system (Figure 5a) was used to measure the aperture and delineate the TCE phase. The system includes a 12-bit charge-coupled device (CCD) camera (AVT Pike F421B) with a spatial resolution of 2048 × 2048 pixels in front of the fracture and a uniform, planar light source (Phlox) producing constant light behind the fracture. The experiment was conducted in a dark box. The fracture were first filled with deionized water and then flooded with at least 100 fracture volumes of 0.0625 g/L FD&C Brilliant Blue #1 dyed water. Light intensities were measured by the sensor of the CCD camera both for the fracture with clean water and with dyed water. To minimize the error due to random noise produced by the sensor, 256 images were taken and averaged each time when the light intensities were measured. The aperture field was then determined by applying the Beer-Lambert law as

$$b = \frac{1}{uC_d} \ln\left(\frac{I_0}{I}\right) \tag{11}$$

where u is the absorptivity of the dye, C_d is the concentration of the dye and I_0 and I are the light intensities measured for the fracture with clean water and with dyed water, respectively. Aperture measurements were obtained for an area of 17.7 cm × 17.7 cm with 1800 × 1800 pixels. The details of the aperture field measurements are summarized in Table 1 while Figure 6a shows a gray image of the measured aperture field. The aperture field approximately follows a normal distribution with a mean of 0.475 mm and a standard deviation of 0.12 mm. The spatial correlation in the aperture field is characterized by plotting the semivariograms. The correlation length in the horizontal (flowing) direction is about 4.1 mm. For the vertical direction, the semivariogram increases with the separation distance and does not reach a plateau. This is because an increasing trend exists for the mean aperture in the vertical direction. More details can be found in Paper **IV**.

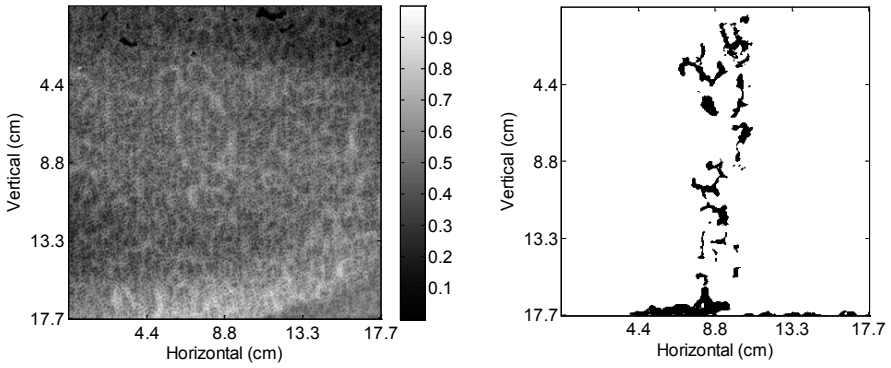

(a) (b)

Figure 6. (a) Measured aperture field; apertures in unit of mm. (b) Initial DNAPL entrapment configuration in the vertical fracture. (Paper **IV**)

Table 1. Properties of the measured aperture field

Parameter	Value and unit
Dimensions	177 × 177 mm
Dimensions, pixels	1800 × 1800
Pixel size	0.0983 mm
Mean aperture	0.475 mm
Standard deviation	0.120 mm
Correlation length, horizontal direction	4.15 mm
Correlation length, vertical direction	Not defined

DNAPL dissolution in a transparent analog fracture

After the aperture field was measured, 1.0 mL TCE was injected from the port on the top boundary using a glass syringe (Hamilton) with a rate of about 0.5 mL/min. The injection created downward fingered flow of TCE which also resulted in entrapped TCE blob along the finger tracks. The difference in light absorbance for the pure TCE and the dyed water provided contrast in light intensities that were captured by the CCD camera. This enabled differentiation of the DNAPL and the dyed water by subsequent image processing. About a half (0.525 mL) of the injected TCE reached the bottom and formed a large continuous blob. The rest of the injected TCE was trapped by capillary forces as residual blobs. Figure 6b shows a binary image of the TCE entrapment configuration. Note that part of the large blob at the bottom was outside of the recorded area by the camera and is not shown in Figure 6b. This large blob will be excluded from the analyses of saturation, interfacial area and mass transfer characteristics. The focus of the experi-

ment was to quantify the dissolution process of the residual DNAPL blobs which showed significant variability in sizes and shapes.

Water (with zero TCE concentration) inflow rate from the left-hand side boundary was kept at 0.1 mL/min during the dissolution. The CCD camera was then programmed to take pictures regularly at an interval of 2 hours. The dissolution experiment was run for 17 days and the evolution of the DNAPL blobs was recorded. The experimental result was used to validate the develop mechanistic modeling approach for DNAPL dissolution as well as to draw conclusions concerning mass transfer characteristics of residual blobs from fingering type of non-wetting phase invasion.

Results and discussion

Effects of single-fracture aperture statistics on DNAPL entrapment and dissolution (Paper **I**)

In order to investigate the effect of fracture aperture characteristics on DNAPL entrapment and dissolution, a series of simulations was carried out by using the continuum model presented previously. The aperture fields were assumed to be log-normally distributed with an exponential autocovariance function. The geometric mean aperture was set at 2.0×10^{-4} m, which is of the order of laboratory measurements of natural granite fractures (Hakami and Larsson, 1996) and dolomitic limestone fractures (Tunnicliffe and Thomson, 2004). When generating the aperture fields, correlation length λ and standard deviation $\sigma_{log\ b}$ (b in unit of m for the base 10 logarithm throughout the thesis) are varied; the base case has λ =18 mm and $\sigma_{log\ b} = 0.2$. For each combination of λ and $\sigma_{log\ b}$, 10 realizations of the aperture field were generated and simulated for entrapment and dissolution. The fracture size was 20 cm × 20 cm with a uniform grid spacing of 2 mm. The continuum-based modeling approach was used for the simulations. Paper **I** provides more details of the simulations.

Two scenarios of boundary conditions for DNAPL entrapment and dissolution were considered. Scenario 1 consists of a vertical, initially water-saturated fracture with (i) TCE source (specified pressure and saturation) on the top boundary and (ii) constant head and prescribed water saturation (= 1) at all other boundaries during TCE infiltration and entrapment. When the TCE migration through the fracture has reached a steady state, the source at the top boundary is removed and the DNAPL in the fracture is allowed to immobilize. This represents a case where pooling DNAPL infiltrates into a fracture and gets entrapped within the fracture by capillary forces. For the dissolution modeling, no flow boundary is assigned both at the bottom and at the top of the fracture and clean water is allowed to flow through the fracture in the horizontal direction. In Scenario 2 the bottom is assigned a no-flow boundary condition during TCE infiltration and entrapment, while the other boundary conditions are the same as for Scenario 1. This scenario represents a case of fracture closure at the bottom and more TCE mass is expected to be trapped in the vicinity of the bottom boundary.

Entrapment

For Scenario 1, the amount of DNAPL entrapped can be seen as representing the ability of the fracture plane to trap DNAPL, as all boundaries are open except the DNAPL source boundary. Example realizations of aperture fields and the corresponding simulated DNAPL entrapment configuration with different aperture standard deviation and correlation length are shown in Figure 7. From these examples one can qualitatively observe that the entrapped DNAPL is in the form of small blobs in cases with λ = 18 mm and $\sigma_{log\ b}$ = 0.1. For larger λ and $\sigma_{log\ b}$ values, DNAPL fingering becomes more pronounced.

In Scenario 2, the lower boundary of the fracture is closed during DNAPL infiltration and entrapment. This scenario represents a fracture which terminates itself without intersection. In this scenario DNAPL gets entrapped both as large continuous blobs near the closed bottom boundary as well as smaller blobs elsewhere in the fracture plane (see Paper **I** for more details).

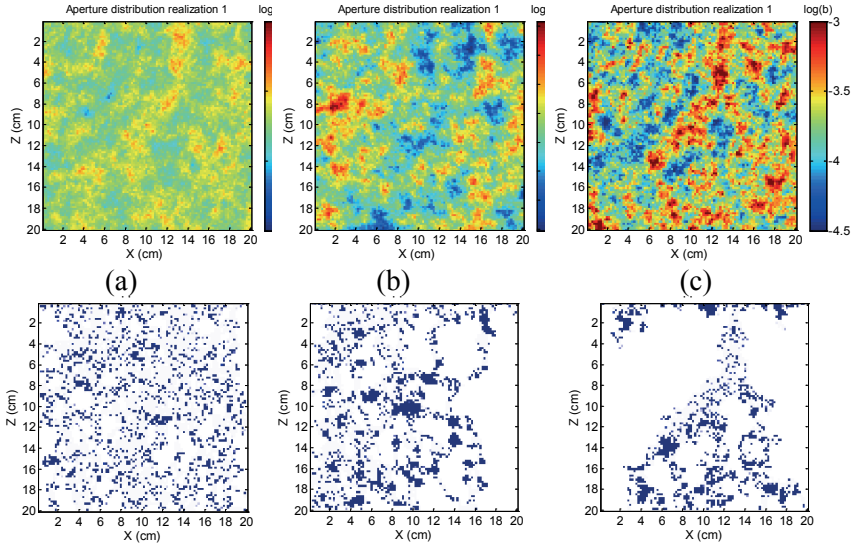

Figure 7. Example realizations of aperture fields with (a) correlation length λ =18 mm, aperture standard deviation $\sigma_{log\ b}$ = 0.1; (b) λ =30 mm, $\sigma_{log\ b}$ = 0.2; (c) λ =18 mm, $\sigma_{log\ b}$ = 0.3 and the corresponding entrapped DNAPL distributions (d, e, f).

The dependence of total entrapped NAPL saturation on aperture standard deviation and correlation length based on all simulations is shown in Table 2. It can be seen from Table 2 that with increasing correlation length ($\sigma_{log\ b}$ is fixed at 0.2) the average entrapped DNAPL saturation S_{ni} decreases. This is not surprising as a longer correlation length provides more possible channels

through the domain. An opposite trend with respect to aperture standard deviation is shown in Table 2, i.e. the larger the aperture standard deviation is (λ is constant 18 mm), the more DNAPL is trapped. This is because larger standard deviation produces more distinct contrasts between small and large aperture regions. An extreme case would be a smooth parallel-plate fracture, in which we expect zero entrapped saturation.

Table 2. DNAPL entrapment characteristics for Scenario 1 (Paper **I**).

Aperture field parameters		DNAPL saturation (S_{ni})		Maximum blob size (cm^2)		Average blob size (cm^2)	
		Mean	Std. Dev.	Mean	Std. Dev.	Mean	Std. Dev.
λ (mm)	6	0.343	0.029	1.65	0.32	0.148	0.010
	18	0.264	0.032	2.83	1.01	0.134	0.019
	30	0.226	0.026	3.88	1.38	0.125	0.016
$\sigma_{log\ b}$	0.05	0.101	0.010	0.39	0.13	0.055	0.003
	0.1	0.184	0.020	1.36	0.51	0.085	0.005
	0.2	0.264	0.032	2.83	1.01	0.134	0.019
	0.3	0.286	0.053	3.67	1.26	0.155	0.035

Characteristics of entrapped DNAPL blob sizes are used to show the effect of aperture statistics on entrapped phase morphology. Here all the entrapped DNAPL blobs from the modeling results were traced for each realization of the aperture fields using an image segmentation algorithm. Maximum blob size and average blob size are calculated; their mean values and standard deviations based on the results from10 realizations in each set of aperture statistics are shown in Table 2. As can be seen, there is a clear trend that both increasing of correlation length and increasing of standard deviation lead to larger maximum blob size (on average), and at the same time, to more variation between realizations. On the other hand, it seems that increasing the correlation length results in a slight decrease in the average blob size.

Entrapped DNAPL dissolution

DNAPL dissolution depends on the aperture distribution, the spatial distribution or morphology of the entrapped phase and aqueous phase velocity (relative rates of advection over diffusion). To describe the progression of dissolution, it is useful to show the evolution of average DNAPL saturation normalized to initial entrapped saturation S_n/S_{ni} and flux-averaged outflow concentration normalized to solubility concentration C_{out}/C_{eq}. Depletion of the DNAPL source attributed to dissolution can be represented by change of

S_n/S_{ni}, and C_{out}/C_{eq} is a measure of effective mass transfer at the fracture scale since the influent concentration is zero.

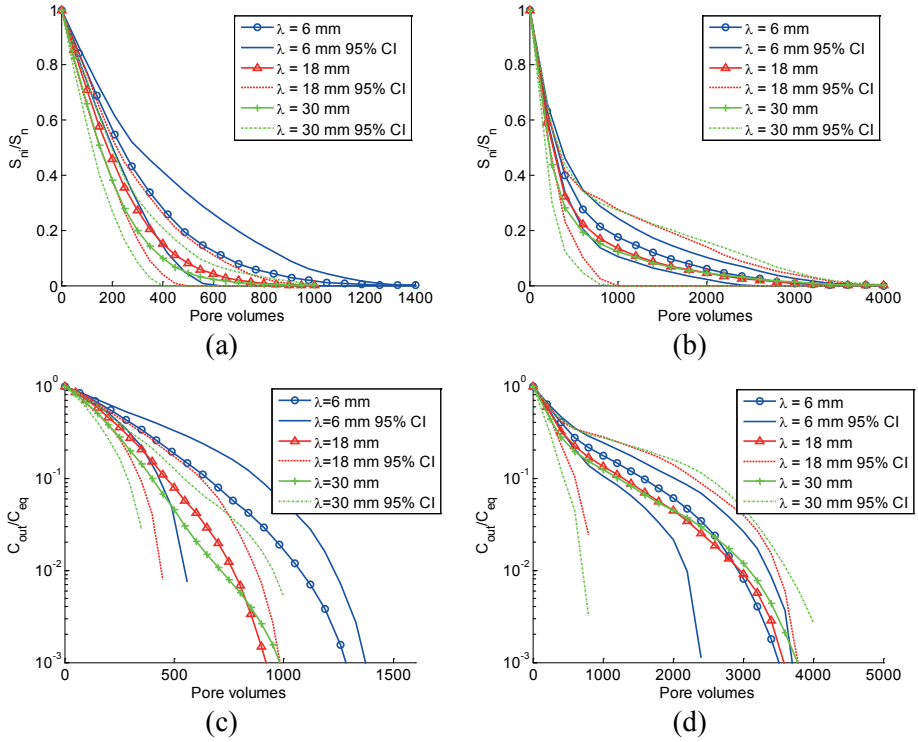

Figure 8. Evolution of normalized saturation (a, b) and normalized outflow concentration (c, d) for different aperture correlation lengths. Figures (a, b, c and d) show the mean and 95% confidence bounds of 10 realizations. Results of modeling of Scenario 1 are shown in (a) and (c). Results of modeling of Scenario 2 are shown in (b) and (d). (Paper **I**)

Results of DNAPL dissolution for different correlation lengths are presented in Figure 8. The figure parts (a, c) show that, on average, with decreasing correlation length more cumulative pore volumes of water (CPV) are needed to fully remove the DNAPL. Complete removal times (not shown in the plots) for realizations with λ =6 mm range between 170 ~320 days, while for realizations with λ =18 and 30 mm the removal times are 100~180 days. Even though longer correlation lengths result in larger maximum blob sizes which may slow down dissolution and increase removal time, here this effect is overshadowed by the fact that on average more DNAPL mass is trapped for realizations with lower correlation length. More initial entrapped mass also leads to smaller average water flow velocity during the dissolution process because of the constant hydraulic gradient through the fracture.

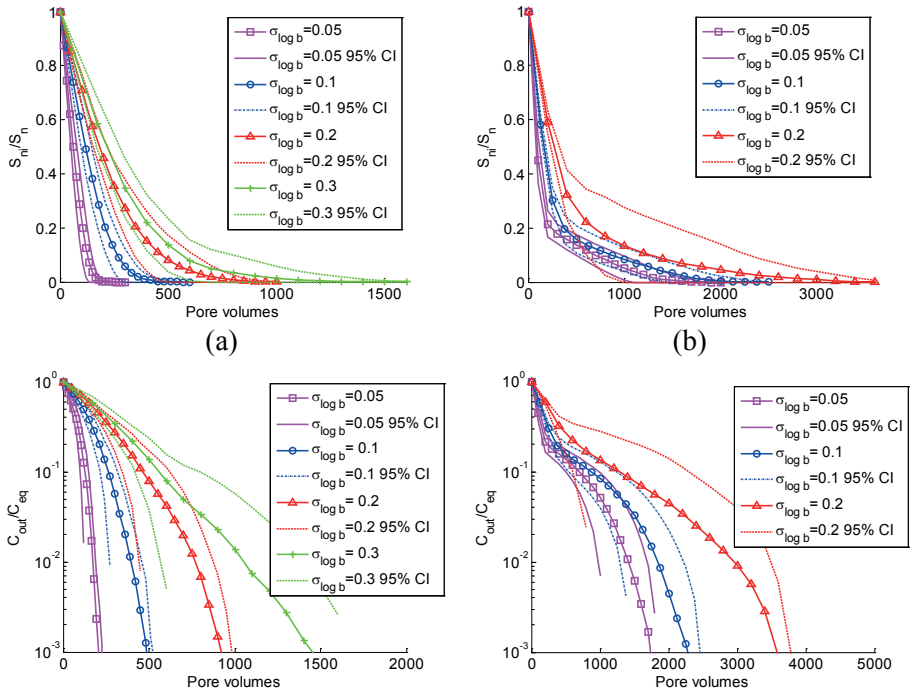

Figure 9. Evolution of normalized saturation (a, b) and normalized outflow concentration (c, d) for different aperture standard deviations. Figures (a, b, c and d) show the mean and 95% confidence bounds of 10 realizations. Results of modeling of Scenario 1 are shown in (a) and (c). Results of modeling of Scenario 2 are shown in (b) and (d). (Paper **I**)

Increasing the aperture standard deviation (aperture variability) leads to on average increasing entrapped mass within the fracture plane. The effect of aperture standard deviation on the dissolution process is shown in Figure 9. For Scenario 1, it is shown in Figure 9(a, c) that realizations with higher aperture standard deviation require larger volume of through-passing water for complete dissolution. Complete removal times (not shown in the plots) for realizations with $\sigma_{log\ b}$ = 0.3 range between 180 ~250 days, and for realizations with $\sigma_{log\ b}$ = 0.1 between 55~70 days. This is because higher $\sigma_{log\ b}$ leads to more entrapped DNAPL mass and, at the same time, larger DNAPL blob sizes. It can also be observed that increasing $\sigma_{log\ b}$ leads to a larger inter-realization variability (wider 95% confidence interval).

For Scenario 2, the bottom boundary is closed during DNAPL migration and entrapment. The DNAPL entrapment in this scenario is featured by large continuous blobs at the bottom of the fracture. From Figure 8(b, d) and Figure 9(b, d) it can be noted that considerably more pore volumes of water and longer dissolution time are needed to completely dissolve the DNAPL com-

pared to Scenario 1. Because of the entrapped DNAPL at the bottom long tails in the effluent concentrations are observed for most of the realizations after the normalized concentration has dropped to about 0.1. The lengths of these tails are related to the amount of DNAPL mass near the bottom. Compared with that in Scenario 1, the average increase in S_{ni} due to the bottom boundary in Scenario 2 is about 4~5%. The extra saturation near the bottom of the fracture in the form of large continuous blobs has led CPV for complete dissolution to become about 1~3 times higher in comparison to Scenario 1. Inspection of the concentration curves in Figure 8 and Figure 9 also shows the qualitative difference in the time evolution between Scenario 1 and 2, which can be used as an indication of interpreting the character of the remaining DNAPL in the fracture.

Source depletion behavior

In order to understand the fracture-scale dissolution behavior, a source depletion function (Parker and Park, 2004; Basu et al., 2008) which links the flux-averaged outflow concentration and the remaining DNAPL saturation is used. The function is based on a simplified analytical solution to 1D steady-state advective-reactive transport equation and a power-law dependence of the effective mass transfer coefficient on the remaining DNAPL mass. It has the form:

$$\frac{C_{out}}{C_{eq}} = 1 - \exp\left[-\alpha \frac{L_s}{K_s} \left(\frac{S_n}{S_{ni}}\right)^{\beta_2} \right] \tag{12}$$

where L_s is the source zone length in the mean flow direction, K_s is the saturated conductivity of the fracture, and α and β_2 are fitting parameters. Equation (12) was fitted to datasets generated from dissolution simulations, each dataset combining results from multiple realizations with the same aperture standard deviation ($\sigma_{log\ b}$) and correlation length (λ). The objective function used for fitting the models was root mean squared error. Fitting parameters α and β_2 were subsequently obtained.

As shown in Figure 10a, for Scenario 1, no significant difference is observed between realizations with different λ, based on visual comparison. The similar behavior for different correlation lengths indicates that the difference in average complete dissolution time for different λ (shown in Figure 8a, c) would only result from the fact that (on average) more DNAPL is trapped in the less correlated aperture fields. For the cases with different aperture standard deviations (Figure 10b) there is a difference. It can be seen that for the same S_n/S_{ni} a larger $\sigma_{log\ b}$ corresponds to smaller mass flux generation, even when realizations with larger $\sigma_{log\ b}$ have more DNAPL mass left in the fracture. This is partly because larger $\sigma_{log\ b}$ leads to bigger DNAPL

blobs (as shown in Table 2), and also because increasing $\sigma_{log\ b}$ (increasing aperture variability) causes more flow channeling through the fracture and thereby more by-passing of the DNAPL entrapment regions.

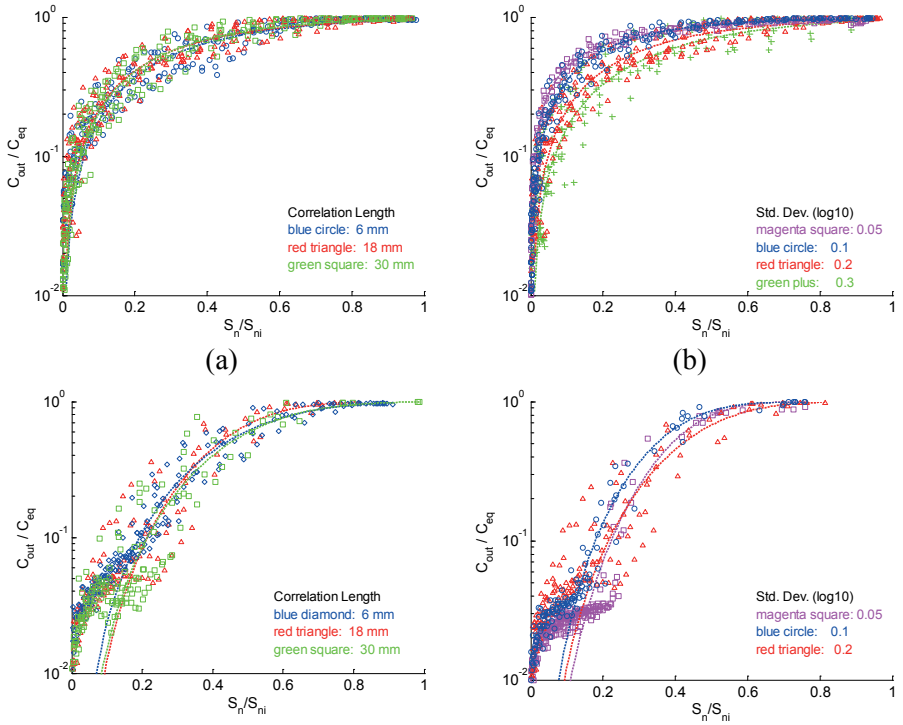

Figure 10. Evolution of normalized concentration as a function of S_n/S_{ni} for different correlation lengths (a, c) and different standard deviations (b, d). a, b for Scenario 1; c, d for Scenario 2. (Paper **I**)

Table 3. Fitted parameters of the simplified source depletion equation. (Paper **I**)

Aperture field parameters		α in Eq.(12)	β_2 in Eq.(12)	RMSE
λ (mm)	6	0.297	1.21	0.073
	18	0.315	1.12	0.074
	30	0.348	1.19	0.061
$\sigma_{log\ b}$	0.05	0.361	0.769	0.029
	0.1	0.435	0.990	0.047
	0.2	0.315	1.12	0.074
	0.3	0.271	1.19	0.089

Parameters fitted to the simple source depletion model are presented in Table 3. The cases with different $\sigma_{log\,b}$ show that increasing aperture standard deviation generally results in increasing β_2. This means that increasing aperture variability slows down the dissolution rate.

In Scenario 2, the entrapment morphology consists of small sparse residual blobs over the fracture plane, as well as large continuous blobs trapped at the bottom. As shown in Figure 10c, d, the simple equation does not capture the long tailing shown in the dissolution profiles at low concentrations due to the large DNAPL blobs at the bottom. To represent the dissolution behavior in this scenario, separate source depletion equations (or step functions) have to be developed for the small sparse blobs over the fracture plane and large continuous blobs at the bottom.

Modeling fluid displacement under the influence of in-plane curvature (Paper **II**)

In order to test the performance of the developed computational algorithm (the ACF approach) for calculating in-plane curvature of an advancing fluid-fluid interface, published experimental data on slow drainage processes in two different fractures (Neuweiler et al., 2004) were used for simulation and comparison. For readability, first a short description of the data is given and then the simulation results and discussion follow. For more details of the drainage experiments, the interested reader is referred to the original publication by Neuweiler et al. (2004).

Experiments

The aperture fields of the two fractures used by Neuweiler et al. (2004) have distinctly different spatial correlation structures, one with a power law variogram and the other with a Gaussian variogram. Following Neuweiler et al. (2004), the two fractures are referred to as the *fractal fracture* and the *Gaussian fracture*, respectively. The horizontal dimensions of the fractures were 0.4 m × 0.4 m. The measured aperture fields have a mean aperture of 0.66 mm and a variance of 0.04 mm^2 for the fractal fracture, and 0.58 mm and 0.02 mm^2 for the Gaussian fracture. The aperture field resolution is 464 × 464 cells for the fractal fracture and 475 × 475 cells for the Gaussian fracture. The two aperture fields are shown in Figure 11(a, b). The fractures were sealed on two opposite ends, while the other two sides were left unsealed as inlets and outlets. The fractures were initially water saturated and then air was allowed to invade and displace the water. The capillary number ($Ca = v\mu_{air}/\gamma\cos\theta$, where μ_{air} and v are viscosity and average velocity for the gas phase) was $\sim 10^{-9}$, which implies capillary dominated flow. The contact

angle was not measured but was estimated to be in the range of 0 ~ 60 degrees in the study by Neuweiler et al. (2004). Pictures were periodically taken to obtain phase distributions during the drainage process. The air phase in the fractures at the breakthrough is depicted in Figure 11(c, d). It can be seen that the air cluster is more compact in the fractal fracture than in the Gaussian fracture. This is due to the difference in the correlation structures of the two aperture fields.

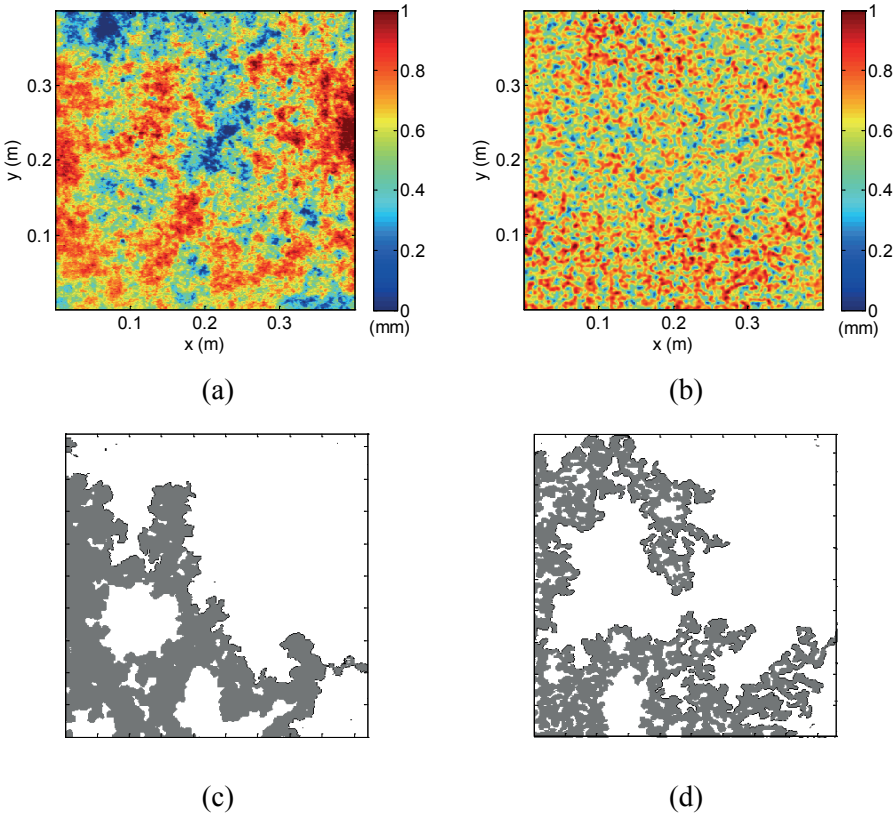

Figure 11. Measured aperture fields and corresponding breakthrough air phase distributions shown in gray. (a, c) fractal fracture; (b, d) Gaussian fracture. Experimental data courtesy of I. Neuweiler. (Paper **II**)

Simulation results

The simulation result from our invasion percolation model with the 'neglecting in-plane curvature' (NIC) approach is shown in Figure 12. Visual comparison shows that neglecting the in-plane curvature yields clusters which are not dense (compact) enough to match the experiment results. In fact, this was shown by Neuweiler et al. (2004) also by comparing a two-point density

correlation function for the air phase. This confirms the importance and need for taking the in-plane curvature into account for these experiments.

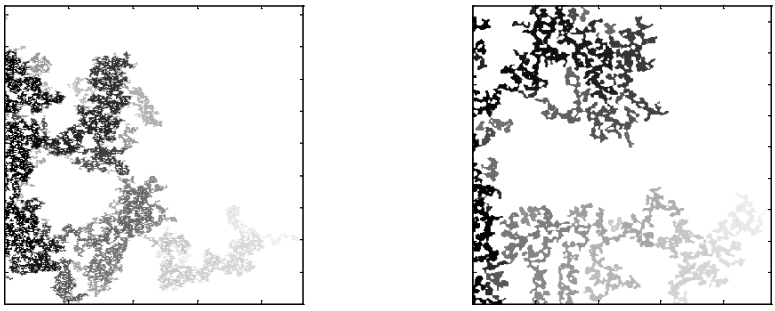

(a) (b)

Figure 12. Measured aperture fields and corresponding breakthrough air phase distributions shown in gray. Darker cells mark a state of earlier times, while lighter cells mark a state of later times. (a, c) fractal fracture; (b, d) Gaussian fracture. (Paper **II**)

In the paper by Neuweiler et al. (2004), the authors used both the model of Glass et al. (1998) and a one-nearest-neighbor model to take the in-plane curvature into account for the simulation of non-wetting phase invasion. Both models reproduced the experimental results well but required defining a length scale for the in-plane curvature prior to the initiation of computational simulation. Here, the ACF approach was implemented in the IP model to simulate the drainage experiments. A threshold value (T) of 0.08 was used for NAE. It should also be pointed out that simulations with $T = 0.1$ were also tested and the results are essentially the same as those with $T = 0.08$. Although the ACF approach finds local curvatures by adaptive circle fitting procedures, a start tracing number n_s needs to be assigned to specify the maximum number of traced interface sites for each local in-plane curvature. The idea is to assign a sufficiently large number for n_s (i.e., to trace sufficiently long distance along the local interface) and let the algorithm determine how many sites are needed for matching a circle that is representative of the local interface curvature. In this study, n_s values of 4, 5 and 6 have been used for the simulations. Note that $n_s = 6$ translates into 11~12 interface sites or an interface length about 10 mm for the two aperture fields. By comparing simulation results from a series of values of n_s, one can also estimate the influence distance along the interface for the in-plane curvature. For comparison purposes, the model of Glass et al. (1998) was also implemented. The contact angle θ was not exactly measured during the experiments but was given a range of 0~60 degrees (Neuweiler et al., 2004), here θ was assumed to be 30 degrees as an initial guess. The effect of contact angle on fluid invasion will be discussed in the end of this section.

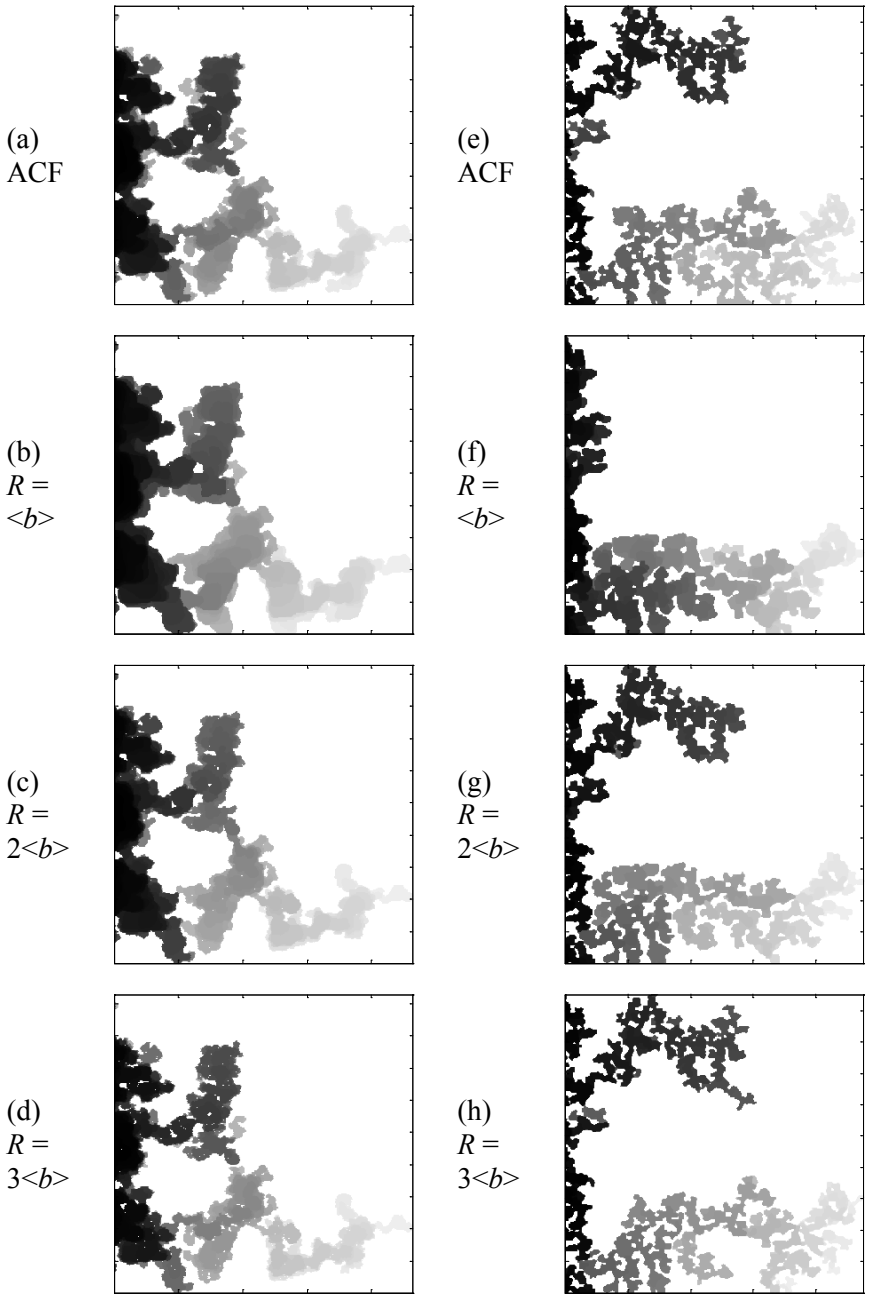

Figure 13. Simulated air clusters and their invasion sequence. Darker cells mark a state of earlier times; lighter cells mark a state of later times. Left panels (a~d): fractal fracture; right panels (e~h): Gaussian fracture. Panels (a, e) are simulated using the ACF approach; Panels (b, c, d, f, g, h) are simulated using the model of Glass et al. (1998) with different length scale parameter R. (Paper **II**)

Figure 13 shows the simulation results using the ACF approach (with n_s = 6 and T = 0.08) and using the Glass et al. (1998) model (with 6 sites on each side of the potential invasion site are traced, and unit vector weighting factor taken as the neighbor number raised to the zeroth power). For the Glass et al. (1998) model, three different values for R (empirical characteristic length scale for in-plane curvature, expressed as multiples of the mean aperture <b>) were used, since no direct quantitative methods exist so far for determination of R. For the fractal fracture (Figure 13a) the air cluster distributions can be very well reproduced by the ACF model, as compared to the experimental result (Figure 11c). Visual inspection shows that the simulations using the Glass et al. (1998) model (Figure 12b, c, d) also present similar results. As a way of quantifying the performance of the simulations, the matching percentage was calculated, here defined as the number of matching sites between the experiments and the simulations divided by the total number of sites. Results of the matching percentage for the simulations are summarized in Table 4. It can be seen that the ACF approach consistently produces better matching than the NIC model and the model of Glass et al. (1998). Note that for the fractal fracture, the simulation results with start tracing numbers of 4, 5 and 6 are very similar to each other. This implies that short-distance configurations on the fluid-fluid interface dominate the influence of the in-plane curvature for this experiment. This is also consistent with the finding of Neuweiler et al. (2004).

Table 4. Properties of the invasion cluster sites with comparison to the experiment clusters. (Paper **II**)

	Exp.	NIC	ACF n_s=6	ACF n_s=5	ACF n_s=4	MoG* R = <b>	MoG* R = 2<b>	MoG* R = 3<b>
fractal fracture								
MP	-	0.834	0.935	0.938	0.938	0.924	0.930	0.927
D_f	1.87	1.73	1.87	1.87	1.87	1.90	1.87	1.85
Gaussian fracture								
MP	-	0.731	0.769	0.757	0.768	0.738	0.768	0.758
D_f	1.82	1.66	1.80	1.79	1.81	1.87	1.83	1.78

MP (matching percentage) is defined as the number of matching sites between the experiment and the simulation clusters divided by the total number of sites. D_f is the fractal dimension of the invasion cluster, calculated by a box counting method. *MoG: Model of Glass et al. (1998).

For the Gaussian fracture (Figure 13e), the overall structure for the invading phase is also well captured by the ACF model. The matching percentages for the simulations can be found in Table 4. Again, the simulation results

with start tracing numbers of 4, 5 and 6 are very similar to each other. The matching percentages are, however, not quite as good as in the case of the fractal fracture. This can be explained by the fact that in the Gaussian aperture field the small correlation length is producing very fine scale invasion patterns that are more difficult to fit in detail with the data resolution available. For the Glass et al. (1998) model, from Figure 13f, g, h it can be observed that the invasion structures become finer and less compact as the parameter R increases from <b> = 0.58 mm to 3<b> = 1.74 mm. Thus, the result for the Glass et al. (1998) model is very sensitive to this pre-defined parameter.

Fractal dimension of the invasion clusters

Invasion phase structures are often irregular or complex and sometimes show self-similarity. For capillary dominated displacement in a two-dimensional fracture, the aperture variability acts to roughen the invasion cluster or to make it fractal, while the in-plane curvature plays an opposite role to make the invasion cluster more compact. The fractal dimension is one way to describe the compactness or complexity of invasion clusters. Here, we focus on the fractal dimension of the entire invasion cluster to study the invasion phase compactness. The fractal dimension of the invasion clusters was measured using the box counting method (Ferer et al., 2004). In the box counting procedure, $N_b(\varepsilon)$ is the number of boxes of side length (l/ε where l is the length of the domain) required to cover the cluster object. The fractal dimension D_f is then calculated from the scaling:

$$N_b(\varepsilon) \sim (1/\varepsilon)^{D_f} \tag{13}$$

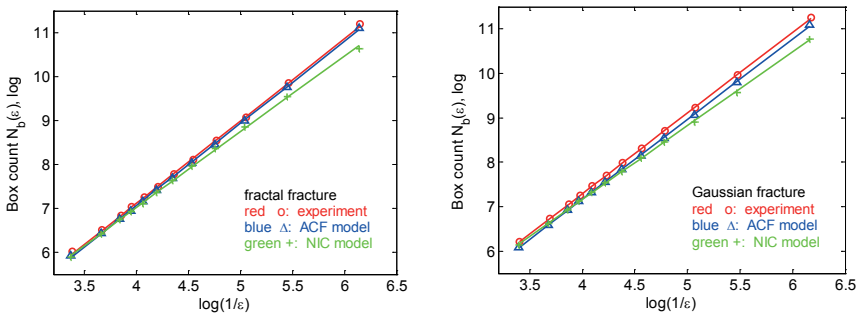

Figure 14. Box counting fractal dimension D_f obtained by the slope of the lines fitted to $\log(N_b)$~$\log(1/\varepsilon)$ points. For the fractal fracture, $D_f = 1.87$ (experiment), 1.87 (ACF), 1.73 (NIC); for the Gaussian fracture, $D_f = 1.82$ (experiment), 1.80 (ACF), 1.66 (NIC). (Paper **II**)

Figure 14 compares both the box counting results of the NIC simulations and of the ACF simulations with the experiments. For both fractures, the NIC model predicts significantly smaller D_f than that of the experiment. This agrees with the earlier observation that neglecting the in-plane curvature results in fluid clusters much less compact to match the experiment. Including the in-plane curvature using the ACF approach produces invasion clusters that can match well with the experiment in terms of fractal dimension.

Table 1 summarizes fractal dimensions for simulated invasion clusters in comparison to the experimental ones. It can be seen that, the simulations with the ACF approach yield D_f very close to the experimental results without pre-assigning any in-plane curvature length scale parameter, whereas the simulations using the Glass et al. (1998) model show that the result is sensitive to the chosen in-plane curvature parameter R.

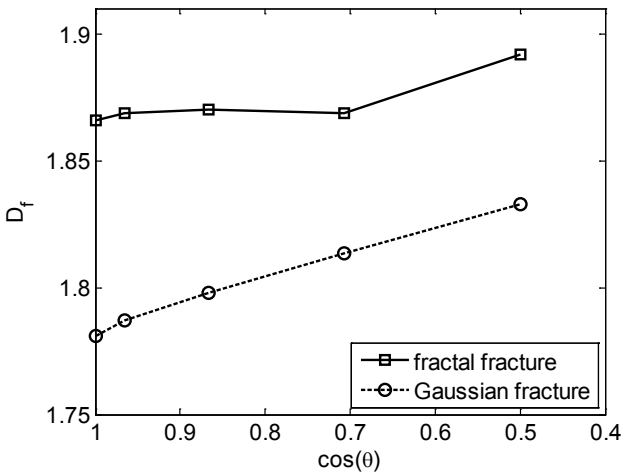

Figure 15. Effect of contact angle on the box counting dimension of the invading fluid clusters. (Paper **II**)

Effect of contact angle

Wetting properties of the fracture walls influence the immiscible displacement process, because the contact angle affects the aperture-induced curvature ($1/r_1$) and thus the relative importance of in-plane curvature $1/r_2$ in comparison to $1/r_1$. Since the contact angle θ was not measured during the experiments, the ACF approach was tested with a series of contact angles from 0 to 60 degrees. Figure 15 shows the effect of contact angle on fractal dimension of invading fluid clusters (D_f). Interestingly, the two fractures exhibit very different behavior. For the Gaussian fracture, it seems that D_f shows a linear dependence on $\cos\theta$. According to this dependence, the D_f value 1.816 observed for the Gaussian fracture experiment corresponds to a contact angle

of about 45 degrees ($\cos\theta = 0.7$). For the fractal fracture, D_f does not seem to be affected by the contact angle for angles below 45 degrees. The different behavior of D_f may be explained by the distinctly different spatial correlation structures of the two fractures. In the Gaussian aperture field, large aperture regions and small aperture regions are well blended, while in the fractal aperture field with a power-law variogram, large apertures (as favored by the invading non-wetting phase) are segregated from small apertures to a much stronger extent. The strong segregation of large apertures in the fractal fracture has a pronounced impact on the shape of the invading fluid cluster. This strong impact can somehow mask the effect of contact angle below 45 degrees.

Comparison of IP and continuum-based models for modeling fluid displacement (Paper **III**)

In the majority of literature addressing immiscible displacement in variable-aperture fractures some type of IP models have been used. Continuum-based models are much less used, mainly as their applicability at this scale is not straight-forward. It is therefore of interest to evaluate these two modeling approaches for studying the flow dynamics and phase structures within a variable-aperture fracture. Such comparison has previously not been presented. In this section, NAPL invasion to an initially water saturated fracture, an example of immiscible displacement, was modeled by using the two approaches. To facilitate the comparison, the focus was put on cases where N_c/δ is small (< 1) so that the aperture-induced curvature dominates over the in-plane curvature. That is, the interface smoothing effect rendered by the in-plane curvature is ignored. Both cases with horizontal fractures and with vertical fractures are considered.

Horizontal fractures

A series of simulations was carried out to compare the aforementioned two approaches for the case of a NAPL displacing water in horizontal fractures where there are no gravity stabilizing/destabilizing effects. A 20 cm×20 cm fracture plane with a grid spacing of 2 mm was used for the simulations. The aperture fields were assumed to be log-normally distributed with an exponential function for spatial correlation. The geometric mean aperture is 1.0×10^{-4} m and the standard deviation $\sigma_{log\ b}$ is 0.15. The isotropic correlation length is 2.4 cm. The model domain has a NAPL inflow boundary (constant NAPL injection rate) on the left, a water outflow boundary on the right (constant water pressure and saturation) and no-flow boundaries on the other two

sides. Initially all fractures are water saturated. The viscosity of the NAPL is 0.566×10^{-3} Pa·s and the NAPL-water interfacial tension is 34.5 mN/m.

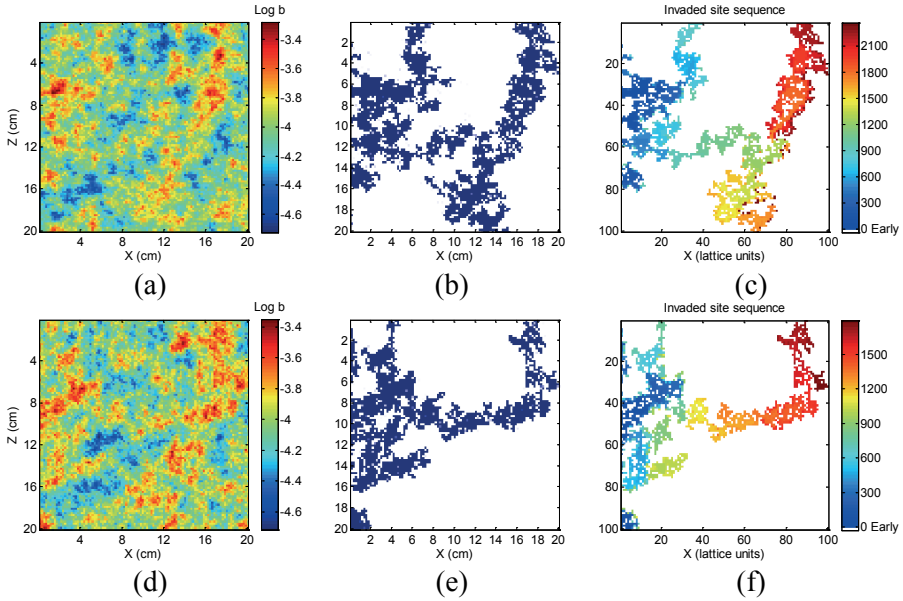

Figure 16. Comparison of the continuum model and the IP model for two example realizations of aperture fields (a, d) of a horizontal fracture. Figure parts (b, e) are for the continuum model (with injection rate 5×10^{-7} kg/s) and (c, f) for IP model invasion sequence. (Paper **III**)

Figure 16 presents two example realizations of the aperture fields simulated with both models. The injection rate 5×10^{-7} kg/s corresponds to a very small capillary number (Ca = $v\mu_n/\gamma\cos\theta$, where μ_n and v are viscosity and average velocity for the NAPL) of the order of 10^{-7}. As can be seen in Figure 16, generally the continuum-based model and the IP model produced very similar patterns for the non-wetting phase (NAPL) invasion. The matching percentage between the continuum-based and IP model (matching percentage here is defined as the number of matched cells over the total number of cells) is over 96%. This means that, for the capillary dominant case here, the differences between the predictions from the continuum-based model and from the IP model are very small (less than 4%). The small capillary number is necessary for direct comparison of the continuum model and the IP model. This is because the IP model ignores viscous forces, whereas, in the continuum model, viscous effects in both fluids are inherently taken into account.

Using the continuum-based model allows one to examine the effect of capillary number (Ca) on non-wetting phase invasion. Increasing capillary number means increasing relative importance of viscous force versus capillary force. The effect of capillary number on non-wetting phase invasion

cannot be done with the IP model, since viscous force is ignored in the IP model. Here the capillary number was varied by applying different injection rates. One of the generated aperture field realizations (Figure 16d) was used and three injection rates 2.0×10^{-6}, 2.0×10^{-5} and 1.0×10^{-4} kg/s have been applied. The corresponding dimensionless capillary numbers are about 1.0×10^{-6}, 1.0×10^{-5} and 0.5×10^{-4}, respectively. As shown in Figure 17a, for the small capillary number case, the non-wetting phase invasion result resembles that of the IP model (Figure 16e). As the Ca increases (Figure 17b), the invasion phase expands to a larger region in the fracture and when the injection rate is high (large Ca, Figure 17c), the invasion phase spans all over the fracture with small trapping zones of the wetting phase. In other words, the invasion phase becomes more and more compact as Ca increases. The non-wetting phase saturation in the fracture (S_n) in the large Ca ($\sim0.5\times10^{-4}$) case is 0.73, which is much higher than the IP result ($S_n \sim 0.36$). It is also interesting to note that the non-wetting phase invasion patterns bear significant resemblance to experimental flow patterns in two-dimensional porous media (Ferer et al., 2005; Frette et al., 1997).

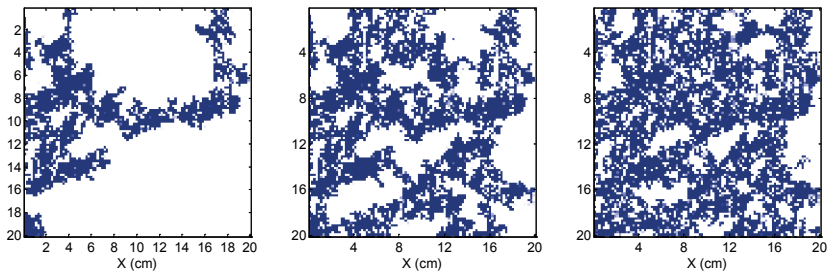

(a) (b) (c)

Figure 17. Effect of capillary number (Ca) on non-wetting phase invasion for a horizontal fracture. (a) Ca = 1.0×10^{-6} (b) 1.0×10^{-5} and (c) 0.5×10^{-4}. The non-wetting phase saturation in the fracture for a, b, and c is 0.36, 0.63 and 0.73, respectively. (Paper **III**)

Vertical fractures

A case of immiscible displacement in vertical fractures where the gravity forces play a role due to the fluid density difference has also been simulated by using both the continuum approach and the IP model. The displacement scenario was a dense non-aqueous phase liquid (DNAPL) penetrating a vertical fracture from the top. The density of the DNAPL is 1462 kg/m^3 and the other properties, model parameters and dimensions are the same as in the horizontal fracture case previously described. The bottom boundary was set to allow free drainage, while the two side boundaries were set as no flow. Initially the fracture was water saturated. In Figure 18(b, c) one can see that,

with very low injection rate (5×10^{-7} kg/s, corresponding to capillary number about 2.5×10^{-7}) the continuum model and the IP model predict very similar pattern for the DNAPL invasion. The matching percentage between the models is 98%. The invasion is characterized by fingering of the DNAPL through the vertical fracture.

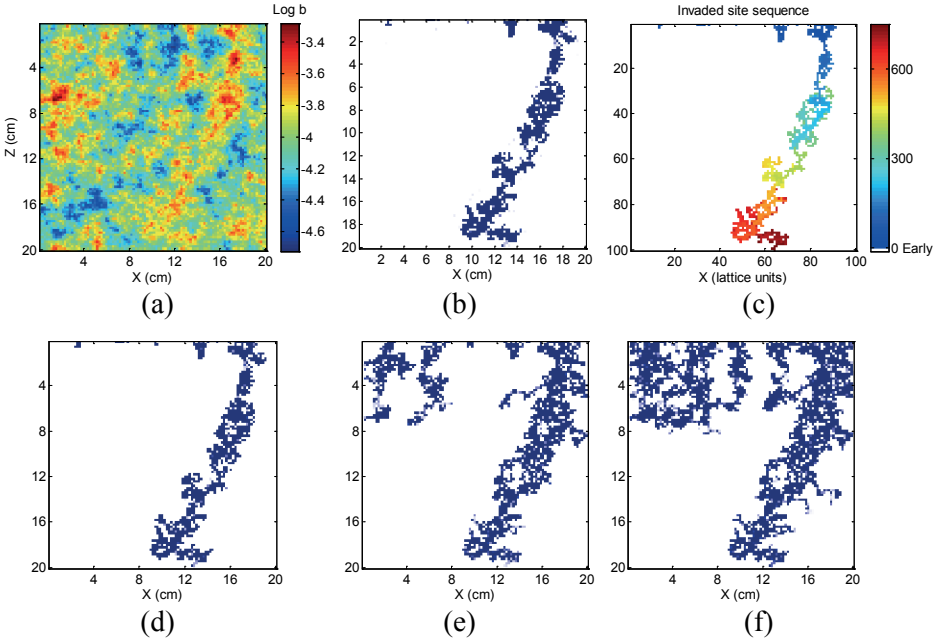

Figure 18. Comparison of the continuum-based model (b) and the IP model (c) for an example realization of aperture fields (a) of a vertical fracture. Figure parts (d~f) are for the continuum model (with injection rates 5×10^{-6}, 5×10^{-5}, 5×10^{-4} kg/s, respectively). (Paper **III**)

When the injection rate is high, viscous forces become significant compared to capillary forces. In this case the invasion patterns as simulated by continuum models are expected to be different from those predicted by the IP model which ignores the viscous force. Experimental observations by Loggia et al. (2009) showed that generally with increasing injection rate, the non-wetting phase invasion pattern changes from single tortuous fingers to clusters with numerous tortuous fingers. We used the aperture field shown in Figure 18a and applied three higher injection rates which correspond to capillary numbers ranging from about 2.5×10^{-6} to 2.5×10^{-4}. Another dimensionless number, Bond number ($Bo = \Delta\rho g\langle b\rangle^2/\gamma$, where $\langle b\rangle$ is the mean aperture), can be used to represent the importance of gravity forces in comparison to the capillary forces. For the case studied here, Bo is equal to 1.3×10^{-3}. According to the phase diagram for stability of displacement presented by Loggia et al. (2009), the values of Ca and Bo correspond to the

gravitationally unstable regime. Results shown in Figure 18(d~f) suggest that, the invasion pattern change from a single dominant finger to multiple fingers, as expected.

Fracture scale capillary pressure-saturation functions

As the continuum-based approach presented above, unlike the IP approach, can be applied to a wide range of NAPL injection pressures, it can also be used to determine the effective (upscaled) capillary pressure-liquid saturation (Pc-S) curves for the fracture-level system. In porous media, the capillary behavior of two-phase flow depends on the contact angle and the pore size distribution. The dimensions and arrangement of the pore bodies and pore throats have a decisive effect on the capillary pressure. Analogously, the capillary pressure-saturation relationships for a variable-aperture fracture are determined by the contact angle and the aperture distribution. Reitsma and Kueper (1994) experimentally measured the Pc-S relationship for a natural rock fracture and found that the relationship could be well represented by a Brooks-Corey capillary pressure function (Brooks and Corey, 1964). Here we constructed the fracture capillary pressure-saturation curve numerically by using the continuum approach. By applying different pressures on the non-wetting phase boundary for the fracture aperture field shown in Figure 16d, we obtained the capillary pressure-saturation curve for the fracture. Here the simulated curve can also be well fitted to both the van Genuchten (1980) and the Brooks-Corey (BC) functions for primary drainage. More details of fitting can be found in Paper **III**.

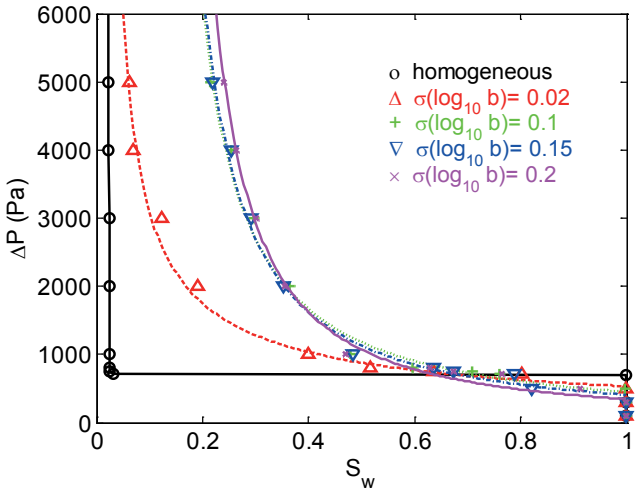

Figure 19. Simulated ensemble averaged capillary pressure – saturation relations (symbols) and best fits of the Brooks-Corey model (red, green, blue and magenta curves) for different $\sigma_{log\ b}$ values. (Paper **III**)

Given the analogy between the pore size distribution of a porous medium and the aperture distribution in a rough-walled fracture, it is of interest to investigate the dependence of the capillary pressure-saturation relationship of a horizontal fracture on its aperture field heterogeneity. In order to study this, the heterogeneity is varied from a homogeneous (parallel-plate) case to a highly heterogeneous case. Specifically, we simulated the fracture scale capillary behavior under cases with different aperture standard deviation ($\sigma_{log\ b}$) values ranging from 0.02 to 0.2. The aperture fields all have the same geometric mean aperture of 0.1 mm and exponential autocorrelation function with an isotropic correlation length of 2.4 cm. Ten realizations of aperture fields were simulated for each of the heterogeneous cases.

It can be seen from Figure 19 that a higher $\sigma_{log\ b}$ results in a larger departure from the behavior of the parallel-plate case with the geometric mean aperture. Increasing $\sigma_{log\ b}$ means higher probability of having large aperture regions close to the non-wetting phase inflow boundary. Therefore, it is easier for the non-wetting phase to enter the fracture when $\sigma_{log\ b}$ is larger. Increasing $\sigma_{log\ b}$ also leads to increased amount of water that is trapped in the fracture, meaning that residual water saturation in the fracture depends on $\sigma_{log\ b}$. The ensemble averaged Pc-S relations were fitted to both the Brooks-Corey and van Genuchten (VG) functions. The fitting parameters are presented in Paper **III**. Figure 19 also shows that Pc-S relations for cases with $\sigma_{log\ b} = 0.1$ and $\sigma_{log\ b} = 0.2$ are very close to each other. This indicates that there may be an asymptotic behavior where further increase from $\sigma_{log\ b} = 0.2$ to a higher value will not lead to significant change in the Pc-S relation.

Dissolution of DNAPLs entrapped as residual blobs and dead-end pools (Paper **IV**)

Residual blobs from DNAPL fingers

A physical experiment on dissolution of residual blobs resulting from DNAPL fingers has been performed. The measured aperture field and the initial DNAPL distribution for dissolution are shown in Figure 6. Tracking the DNAPL volume during the dissolution experiment was done by continuous monitoring of the DNAPL distribution by the CCD camera. The residual DNAPL saturation (S_{nr}) is defined as the DNAPL volume in the form of residual blobs divided by the fracture volume. Figure 20a presents the evolution of S_{nr} over the dissolution period. During the 17-day dissolution experiment S_{nr} dropped from 0.034 to 0.0065. It can be seen in Figure 20a that the rate of S_{nr} decrease gradually reduces. This reflects the fact that the specific DNAPL-water interfacial area (a_i) decreases with S_{nr} as is evident in Figure 20b. Note that the specific interfacial area here was not a direct measurement

and does not include the interface between the DNAPL and the water films along the fracture walls. Rather, we estimated the interfacial area by integrating the measured apertures along the DNAPL perimeters from the DNAPL-water binary images, following the method by Detwiler et al. (2001). Numerical simulations by Detwiler et al. (2009) revealed that a_i can be approximated as a linear function of DNAPL saturation for a wide range of saturation values. Here, it is shown in Figure 20b that, for small saturation values corresponding to finger residual blobs in this study, a linear relationship also well describes the S_{nr} - a_i data, while a power law relationship (a_i = 6.37 $S_{nr}^{0.8}$) fits the data slightly better.

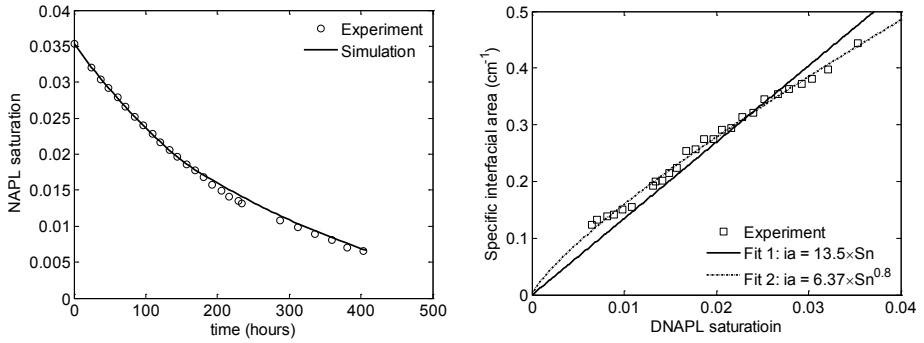

(a) (b)

Figure 20. (a) Change of residual DNAPL saturation (S_{nr}) over the duration of the dissolution experiment. (b) Specific interfacial area as a function of the residual DNAPL saturation. (Paper **IV**)

Table 5. Parameters for simulation of the dissolution experiment

Parameter	Value and unit
Grid dimension	900 × 900
Grid spacing	0.197 mm
Molecular diffusion coefficient (D_m) [a]	9.3×10^{-10} m^2/s
TCE density [b]	1.465 g/cm^3
Solubility (C_{eq}) [a]	1.28 g/L
TCE-water interfacial tension [b]	0.0345 N/m
Contact angle [c, d]	48 °

References: a, Detwiler et al. (2001); b, Mercer and Cohen (1990); c, Glass et al. (1998); d, Liechti et al. (1997).

The DNAPL dissolution in the measured aperture field was also simulated by using the computational algorithm described in the *Modeling* section. The experimentally measured DNAPL distribution (Figure 6b) was used as the initial condition. The simulation parameters are presented in Table 5. The relevant boundary conditions for the flow simulations were specified accord-

ing to the experimental condition, i.e., constant water flux along the inflow boundary, constant pressure along the outflow boundary and no flow boundaries for the other two sides parallel to the mean water flow direction. The water inflow rate was 0.1 mL/min. The boundary conditions for the transport simulations were zero concentration at the inflow boundary, $\partial C/\partial x = 0$ at the outflow boundary and no flux for the other two sides. Figure 20a presents the simulated S_n reduction by dissolution in comparison to the experimental data. It can be seen that the modeling approach for DNAPL dissolution gives results that closely follow the experimental observations. Comparison of the blob shapes and the interfacial area between the simulated and experimental results also showed good agreement (not shown), which further supports the contention that the physically-based modeling approach (linking flow and transport with interphase mass transfer and physically based entrapped blob shrinkage) can realistically simulate DNAPL dissolution in vertical variable-aperture factures.

The water flow velocity through the fracture influences the dissolved TCE concentration field and thus the local interphase mass transfer which is driven by the concentration gradient at the immediate vicinity of the fluid-fluid interface. It is therefore of interest to quantify the effect of water velocity on the mass transfer at the fracture scale. The good agreement between the simulated and experimental results of the DNAPL dissolution also supports the further use of the dissolution modeling approach for investigation of mass transfer under different water flow rates.

It is useful to represent the fracture-scale interphase mass transfer by a set of simple constitutive relationships of the specific interfacial area a_i and the dimensionless Sherwood number *Sh*. The Sherwood number *Sh*, defined as $Sh = k_i\langle b\rangle/D_m$ where $\langle b\rangle$ is the mean aperture and k_i is the intrinsic mass transfer rate coefficient, was shown by Detwiler et al. (2009) to be only dependent on water flow rate for the case of entrapped residual blobs from the imbibition process under gravity neutral and stabilized conditions.

In this study, DNAPL dissolution was simulated for different flow rates ranging from 0.005 to 2.5 mL/min. These flow rates correspond to dimensionless Peclet numbers (*Pe*, which weighs the relative magnitude of advective to diffusive transport and is defined as $Pe = q\langle b\rangle/D_m$, where q is the average water flow velocity) from about 0.6 to 295. In order to quantify the dependence of the mass transfer rate coefficient on the flow rate, we applied the simplified analytical solution to 1-D steady-state advective-reactive transport equation (Parker and Park, 2004) to the initial steady-state flow and transport solution. The simplified equation is:

$$\frac{C_{out}}{C_{eq}} = 1 - \exp\left(-\frac{KL_s}{q}\right) \tag{14}$$

where C_{out}/C_{eq} is the flux-weighted outflow concentration normalized to solubility concentration, K is the bulk mass transfer rate coefficient and is often used to represent the product of k_i and a_i, and L_s is the source zone length in the mean flow direction (L_s is 3.9 cm for experimental entrapment configuration). Rewriting equation (14) in terms of *Sh* and *Pe* yields:

$$Sh = \frac{-Pe}{a_i L_s} \ln(1 - \frac{C_{out}}{C_{eq}}) \ . \tag{15}$$

It should be noted that C_{out}/C_{eq} is also dependent on *Pe*. For sufficiently small *Pe* so that the diffusion transport dominates over the advective transport, C_{out}/C_{eq} is expected to be close to 1. For example, the lowest flow rate considered (*Pe* = 0.6) gives a value of 0.90 for C_{out}/C_{eq}. Using the simulated C_{out}/C_{eq} values, *Sh* is plotted against *Pe* as shown in Figure 21. For *Pe* <20, *Sh* increases fast with increasing *Pe*, meaning that mass transfer in this range of *Pe* values is limited by the advective transport of the dissolved mass. The increasing trend slows down as *Pe* becomes larger, suggesting diffusion limited mass transfer is more and more pronounced.

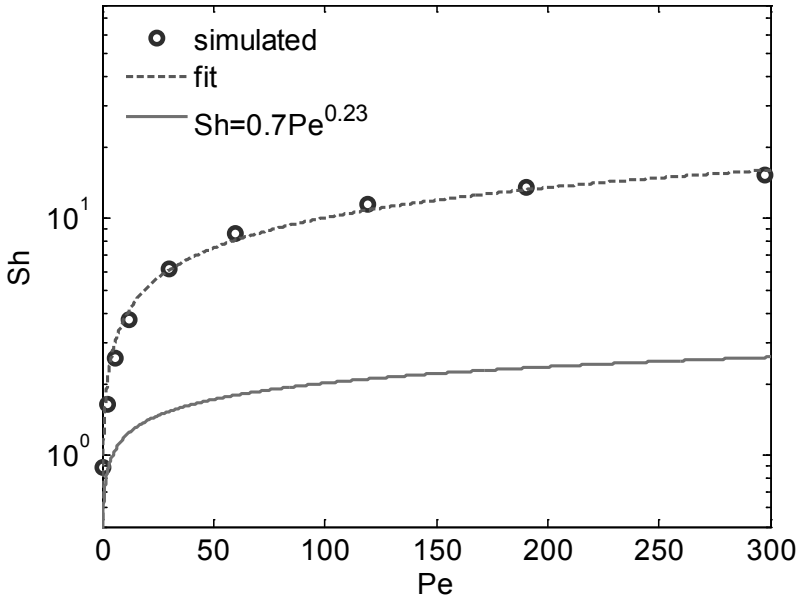

Figure 21. Simulated relationship between *Pe* and *Sh* (circles) and a fitted curve $Sh = 1.43Pe^{0.43}$ (dashed line) in comparison to the relationship (solid line) obtained by Detwiler et al. (2009).

The simulated *Pe*-*Sh* relationship can be well fitted to the following simple power-law equation:

$$Sh = \alpha_1 Pe^{\alpha_2} \tag{16}$$

with the best fitted parameters α_1 = 1.43 and α_2 = 0.43. Figure 21 shows that the Sherwood numbers obtained from this study are significantly larger than those presented by Detwiler et al. (2009). However, it needs to be pointed that the dissolution conditions/scenarios differ in the following respects: (i) the residual blobs result from gravity fingering in this study with $S_{nr} < 0.04$, while the DNAPL entrapment in Detwiler et al. (2009) is obtained from imbibition process under gravity neutral or stabilized condition ($S_{nr} > 0.15$); (ii) the mean aperture (<b> = 0.47 mm) is much larger than that (<b> = 0.2 mm) in Detwiler et al. (2009). However, it should be noted that the difference in mean aperture is only a factor of about 2 but the difference in *Sh* is almost an order of magnitude for larger *Pe* values. The difference in the dependence of *Sh* on *Pe* may reflect the importance of entrapment condition on mass transfer characteristics.

Entrapped DNAPL in a dead-end fracture

DNAPL entrapment in a square dead-end fracture was also considered. In this scenario the lower halves of the side boundaries are closed and the DNAPL gradually fills the dead-end fracture until it reaches the open part of the side boundaries. The DNAPL entrapment configuration is presented in Figure 22; the initial entrapped DNAPL saturation S_n in the fracture is 0.44. Subsequently, DNAPL dissolution was simulated by introducing water inflow from the upper half of the left-hand side boundary and allowing water discharge from the upper half of the right-hand side boundary. The other parts of the boundaries were set to be no flow. The parameters used for the dissolution are the same as those listed in Table 2 except that the fracture dimension is 15.3 cm × 15.3 cm and the grid spacing is 0.3 mm.

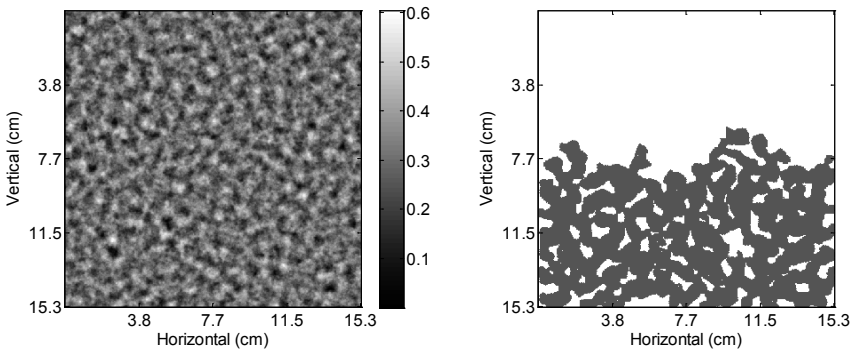

Figure 22. (a) Synthetic aperture field in unit of mm for the dead-end fracture. (b) Simulated DNAPL Entrapment in the dead-end fracture. (Paper **IV**)

Entrapped pool dissolution was simulated for four water flow rates ranging from 0.01 mL/min to 1.0 mL/min. As the DNAPL pool dissolves, the contact interface between the DNAPL and flowing water gradually lowers itself towards the bottom of the fracture because of gravity effects. The contact interfacial area remains more or less constant as DNAPL saturation S_n decreases, unlike in the case of residual DNAPL blobs. We define a depth (d) of the contact interface as the distance in the vertical direction between the mean contact interface and the middle line (which is at the top of the dead-end part of the fracture). This depth increases linearly with decreasing S_n.

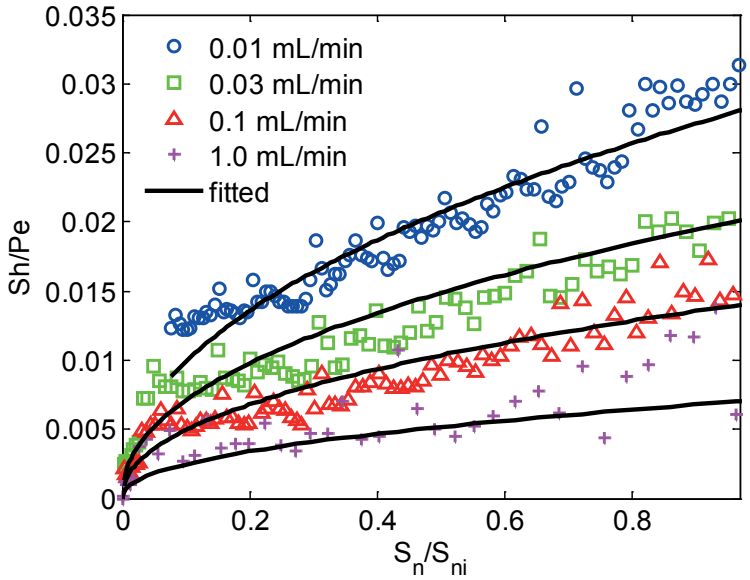

Figure 23. Simulated relationship between S_n/S_{ni} and Sh/Pe for the dead-end pool case. The lines are fitted using equation (17). (Paper **IV**)

The evolution of remaining DNAPL mass and normalized flux-averaged outflow concentration C_{out}/C_{eq} was analyzed. Results (Fig. 8, Paper **IV**) show that generally C_{out}/C_{eq} decreases with increasing depth of the contact interface. This is because it is less efficient for the water flow to 'pick up' the dissolved mass when the contact surface is deeper, not because the contact interfacial area is getting smaller. Based on the C_{out}/C_{eq} data for different flow rates, the Sherwood numbers were calculated according to equation (15). The four different flow rates correspond to Peclet number from about 2.3 to 233. Figure 23 presents plots of Sh/Pe (= $-\ln(C_{out}/C_{eq})/\ a_i L_s$) against S_n/S_{ni} for different Pe values. A simple power-law equation was used to fit the simulated data. The equation is:

$$Sh = \beta_1 Pe^{\beta_2} \left(\frac{S_n}{S_{ni}}\right)^{\beta_3} \tag{17}$$

with best-fit parameters β_1 = 0.37, β_2 = 0.70 and β_3 = 0.46. The fitted lines using these parameters show that the equation can reasonably well describe the dissolution process for different flow rates (Figure 23). By comparison with the case of residual blobs we can also see that the *Sh* values are at least an order of magnitude smaller for any given Peclet number, indicating slower mass transfer for the case of dead-end pools.

It is also interesting to compare the mass flux – source depletion response for the two entrapment scenarios. For the case of residual blobs, the bulk mass transfer rate coefficient (product of intrinsic mass transfer and specific interfacial area) will be related to the amount of remaining mass with an exponent close to 1 as the interfacial area can be approximated by a linear function of saturation. While for the case of dead-end pool, the exponent to the term of remaining mass will be much smaller (0.46 as shown in equation 17 for intrinsic mass transfer), since the interfacial area will be largely insensitive to mass depletion.

Summary and Conclusions

Multiphase flow and transport in fractured rock is of importance to many practical and engineering applications. In the field of groundwater hydrology an issue of significant concern is the release of immiscible organic liquids. It is important to be able to predict both the spatial extent and distribution of these liquids as well as their dissolution kinetics. This thesis addresses two fundamental processes, namely fluid displacement and interphase mass transfer, both pertinent to any predictive modeling of the behavior of the multiphase contaminants in fractured rocks. The focus is in improving the current understanding and capability to model these processes at the scale of individual fractures, the building blocks of any large scale models for fractured media. The work has consisted of conceptual and numerical modeling and model development as well as dedicated laboratory experiments. In the following, the main findings and conclusions are summarized.

In the first part (Paper **I**), effect of fracture aperture characteristics (described through the statistical properties of the aperture distributions) on DNAPL migration, entrapment and dissolution within a variable-aperture fracture has been investigated. The results show that increasing the standard deviation and/or decreasing the correlation length leads to more entrapped DNAPL mass. For a given correlation length the entrapped saturation increases with increasing aperture standard deviation as does the variability in the entrapped saturation between realizations. On the other hand, for a given standard deviation the entrapped saturation decreases with increasing correlation length. Entrapped maximum blob size increases both with increasing aperture correlation length and increasing aperture standard deviation. The initial entrapped DNAPL saturation and structure of the entrapped phase resulting from different correlation lengths and standard deviations strongly influence the dissolution processes. Slower dissolution time is seen both with increasing aperture standard deviation and decreasing correlation length.

The relationship between the outflow concentration, as an indicator for the dissolution mass transfer rate, and the remaining DNAPL mass has also been studied. A simplified source depletion function is sufficient to describe the dissolution process for open fracture cases where DNAPL entrapment is controlled by the fracture aperture topography. The parameters for the source depletion function are not especially sensitive to variations in aperture correlation length. On the other hand, the results reveal that with increasing aperture standard deviation the same outflow solute concentration can corre-

spond to significantly larger amount of NAPL mass remaining in the fracture. In other words, the same average amount of NAPL mass produces smaller solute concentrations in cases with larger aperture variability. Boundary conditions, representing how the fracture is connected to other fractures in the network, also have a large impact on DNAPL entrapment and dissolution. A closed boundary at the bottom leads to large continuous blobs, which cause significant tailing for dissolution. This scenario cannot be adequately represented by the simplified source depletion function but will require alternative models describing the two stages of dissolution, first from the scattered residual blobs and then from the large pooling blobs.

In the second part (Paper **II**), a novel approach - the adaptive circle fitting (ACF) approach – has been developed for calculating the in-plane interfacial curvature for simulating quasi-static drainage in rough-walled fractures. In the ACF approach, local fluid-fluid interfaces are adaptively fitted by osculating circles to determine the in-plane curvature, which contributes to the local capillary pressure. The ACF approach adaptively determines a suitable number of traced sites (or a suitable distance along the interface) for each local interface segment for calculating the in-plane curvature. The approach is adaptive to local interface configuration, while the previous approaches always use the same predefined distance along the interface for the entire fracture. Implemented into an invasion percolation model, the developed ACF approach was applied to fluid displacement simulations against previously published experimental data (Neuweiler et al., 2004). The comparison of the experiment results and the simulations with the ACF approach shows that the experimental results can be well reproduced, in terms of both the matching percentage and the fractal dimension of the invasion phase clusters. Neglecting the in-plane curvature (as in standard IP modeling) in the simulations yields invasion clusters not compact enough to match the experimental results, which demonstrates the importance of in-plane curvature for these cases.

In the third part (Paper **III**), a continuum-based model is presented capable of simulating fluid displacement at the scale of a single variable-aperture fracture and the performance is compared to that of an IP model. The comparison shows that simulations using the continuum-based approach in which the full two-phase mass continuity equations are solved can well reproduce the IP modeling results for the capillary dominant (low capillary number) displacement. Moreover, unlike the IP models, the continuum-based model can also be applied for simulating high-capillary number displacement, since the viscous pressure loss in both phases is inherently accounted for. In addition, the continuum-based model may be applied to displacement with slightly miscible fluid pairs (e.g. CO_2-brine) and to three-phase flow conditions (an example is NAPL migration in a partially saturated fracture). However, the continuum-based approach is computationally demanding and thus is limited to relatively smaller grids. The capability of

the continuum model to simulate gravity driven flow with larger Bond numbers remains to be further investigated. On the other hand, the IP model is computationally appealing, and allows for a more convenient incorporation of the effect of in-plane curvature (See Paper **II**). IP models may also be extended to include first order approximation of the viscous (pressure loss) effect. Analyses using such extensions can be found in recent literature (e.g., Xu et al., 1998; Ferer et al., 2011). It is noted that further model development is needed for understanding the complex physics associated with the sometimes observed phenomena such as fragmentation, pulsation, film flow in gravity destabilized flows (e.g., Meakin et al., 1992; Glass and Yarrington, 2003).

In the last part (Paper **IV**) DNAPL dissolution in a variable aperture fracture under two entrapment configurations, namely, trapped residual blobs from gravity fingering and trapped pools in a dead-end fracture, has been investigated. A physical dissolution experiment of residual DNAPL blobs in a vertical analog fracture using light transmission techniques has been performed. The experimental results show that the specific DNAPL-water interfacial area decreases approximately linearly with DNAPL saturation. A high-resolution mechanistic (physically-based) numerical model has been developed which is able to excellently reproduce the experimentally observed DNAPL dissolution process. The model has been applied to simulate dissolution of the residual blobs under different water flushing velocities. The simulated relationship between the Sherwood number *Sh* (representing intrinsic mass transfer rate coefficient for a given fracture) and Peclet number *Pe* (representing the relative magnitude of advection to diffusion) can be well fitted with a simple power-law function ($Sh = 1.4Pe^{0.43}$). To investigate mass transfer characteristics of entrapped dead-end pools, numerical modeling of entrapment and dissolution of DNAPL in a vertical dead-end fracture has also been carried out. As the pool dissolves, the depth of the interface between the DNAPL and the bulk of the flowing water linearly increases with decreasing DNAPL saturation. The increasing depth of the contact interface causes the flowing water to become less and less efficient in 'picking up' the dissolved chemical, suggesting the dependence of the mass transfer rate on the interface depth, or alternatively, the remaining DNAPL saturation in the fracture. Simulation results show that, for a given Peclet number, the resultant Sherwood number *Sh* is significantly smaller than that in the case of residual blobs, indicating slower mass transfer. The results also show that the *Sh* can be well fitted with a power-law relationship as a function of *Pe* and remaining mass percentage.

Finally, some future research topics relevant to the theme of this thesis can be suggested. These topics cover both a further understanding of the small scale physical behavior as well as large, fracture-network scale modeling. The most relevant topics include: (i) further understanding of multi-fluid dynamics under general conditions where the combined effect of capillary,

viscous, gravitational and inertial forces shapes the phase structures which may be compact, or fractal, or highly channelized; (ii) the role of fracture intersections and their topological variations on multiphase flow and contaminant transport; (iii) the effect of anisotropic aperture fields on fluid displacement, mass transfer and solute transport; and (iv) predictive modeling of multiphase flow and contaminant source depletion at the field scale at the level of large scale fracture networks.

Acknowledgements

First I would like to thank my main supervisor Auli Niemi who offered me the opportunity to pursue my graduate studies at Uppsala University. I am grateful for her scientific support and advice during my time as a PhD student and also for her encouragement for my research work. Her continuous effort throughout my PhD studies from getting me started to finishing this thesis is appreciated. I am also grateful to my assistant supervisor Fritjof Fagerlund who is always available for valuable discussions and advices as well as practical help. He is also specially thanked for translating the summary and abstract of this thesis from English into Swedish. I also would like to specially thank my other assistant supervisor Tissa Illangasekare at Colorado School of Mines. Despite the long distances, he has traveled several times to meet with us for discussions which turned out to be fruitful. He is also thanked for giving me an opportunity to visit his lab to learn experimental experiences and skills. He has also helped in many other aspects during my six-month stay at CSM. Additionally, his academic achievements have been and will continue to be inspirational to me.

The Swedish Research Council (Vetenskapsrådet) through grant 2007-4765 is gratefully acknowledged for the financial support to this work.

I thank Chin-Fu and Yvonne Tsang for many stimulating scientific discussions which were helpful for my research work. All colleagues in the geohydrology group at Geocentrum are also thanked for interesting discussions and seminars. I am grateful to Chongyu Xu for spreading the information of the PhD study opportunity to me back in 2008. I also thank Russell Detwiler at University of California, Irvine for sharing his experience on experimental work during my visit in his lab. I would also like to acknowledge Insa Neuweiler at University of Hannover for kindly providing her experimental data to us for Paper II. Thanks also go to Jinsheng Wang and Yanguo Teng (Beijing Normal University) who, as my supervisors for my master's study, introduced me to the field of groundwater hydrology.

I am thankful to all staff at Department of Earth Sciences, including all my present and past fellow PhD-students for the great time I had. Special thanks to Martin for being the best officemate and various practical help. Thanks for friendship and many happy gatherings to Lebing, Liang, Fuguo, Diana, Agnes, Bea, Jose-Luis, Peng Y, Peng H, Fengjiao, Can, Maria, Kristina, Ida, Elias, Carmen, Anna, Eduardo, Estuardo, Michael, Joe, and many more. I thank Roger, Rajinder, Allan and Sven for the advices in research

and teaching work. Thanks to Tomas for the help in the computer matters, and to Inger and Sören for the help in the lab. Anders Ljungberg is thanked for the help in the fracture cell design. There are also many more people that have helped me than I can mention here. I thank all my friends within the department and outside the department.

I thank Mali and Tissa for accommodation of more than a week when I first arrived in Colorado. I enjoyed very much the time and the delicious food Mali made. I also thank Mia for sharing her nice apartment during my visit at CSM. Thanks to Chit, Toshi, Bitao, Ben, Kate, Menka and Abdullah for the various help.

I would like to express my deep gratitude to my family. My parents, you are the best parents in the world! Your great support over many years can never be thanked enough. The belief you always have in me is an invaluable asset for a life time. I am grateful to my elder brother and sister-in-law for the care and support. I also want to thank my wife's family for being supportive.

Last, and most importantly, I am in debt to my dear wife Shang. Without your unconditional love and tremendous support this thesis would have been impossible. I feel like the happiest person with you around. Your smiles make all my hard work worthwhile.

I dedicate this thesis to my wife and my parents.

Sammanfattning på svenska (Summary in Swedish)

Flerfasflöde och ämnestransport i sprickigt berg är viktigt för många praktiska och tekniska problem. Utsläpp av tunga, svårlösliga organiska vätskor (engelska: dense non-aqueous phase liquids: DNAPLs; t.ex. klorerade lösningsmedel) till vattenresurser i sprickigt berg utgör ett viktigt miljöproblem inom grundvattenhydrologin. Det är av praktisk betydelse att kunna beräkna spridningen av organiska vätskor i sprickiga akviferer samt deras lösningstakt till grundvattnet. Denna studie behandlar två fundamentala processer som är avgörande för prediktiv modellering av flerfasföroreningars spridning i sprickiga medier – utbredning av den organiska vätskan och massöverföring mellan organisk vätska och vatten. Arbetet fokuserade på att förbättra nuvarande kunskap om fysikaliska processer på liten skala (enskilda sprickor) genom en kombination av numerisk modellering, laboratorieexperiment och modellutveckling. Nedan summeras resultat och slutsatser från avhandlingen.

I artikel **I** undersöktes effekterna av sprickaperturens variabilitet, beskriven med standardavvikelsen hos logaritmerad apertur och rumslig korrelationslängd, på fastläggning och lösning av organisk vätska i en vertikal spricka med varierande apertur. Resultaten visade att högre standardavvikelse och kortare korrelationslängd ledde till att en större volym organisk vätska fastnade i sprickan. För en given korrelationslängd ökade mättnadsgraden av fastlagd organisk vätska med ökande standardavvikelse samtidigt som även variabiliteten mellan olika realiseringar av aperturfältet också ökade. Kortare korrelationslängd ledde också till mer fastläggning av organisk vätska för en given standardavvikelse. Volymen på den största fastlagda förekomsten av organisk vätska (immobil organisk vätska omsluten av grundvatten) ökade både med ökande korrelationslängd och ökande standardavvikelse hos sprickaperturen. Strukturen och morfologin hos den fastlagda organiska vätskan som blir resultatet av olika korrelationslängder och standardavvikelser hade stor påverkan på lösningsprocessen. Större standardavvikelse och kortare korrelationslängd gav långsammare lösning av den organiska vätskan i scenariot med öppet randvillkor på sprickans botten.

Relationen mellan löst koncentration i utflödande vatten och kvarvarande mängd organisk vätska studerades också som ett mått på massöverföringstakten vid lösningen. En förenklad funktion för utmattningen av källan till

löst koncentration i grundvattnet var tillräklig för att beskriva lösningsprocessen i en spricka med öppna ränder där fastläggningen av organisk vätska styrdes av sprickaperturstopografin. Parametrarna i källutmattningsfunktionen var inte känsliga för variation i aperturens korrelationslängd. Å andra sidan visade resultaten att för ökande standardavvikelse hos aperturen kunde samma utflödeskoncentrationer fås med betydande skillnader i kvarvarande mängd organisk vätska i sprickan. Med andra ord, samma mängd organisk vätska producerade lägre koncentrationer i utflödande grundvatten då variabiliteten i apertur var större. Randvillkor som beskriver hur sprickan är ansluten till andra sprickor i ett spricknätverk hade också stor påverkan på fastläggning och lösning av den organiska vätskan. En stängd rand på sprickans botten ledde till stora sammanhängande förekomster av immobil organisk vätska, vilka orsakar ett lösningsförlopp som blir utdraget i tiden. Detta scenario kunde inte beskrivas väl med den förenklade källutmattningsfunktionen.

I artikel **II**, presenterades en ny metod – den adaptiva cirkelpassningsmetoden (ACF – adaptive circle fitting) – som tar hänsyn till krökningen hos gränsytan mellan de två fluiderna (här vatten och organisk vätska) även i riktningen parallellt med sprickplanet vid simulering av kvasistatiska dräneringsprocesser i skrovliga sprickor. Metoden identifierar de cirklar som bäst beskriver gränsytans krökning lokalt vilket ger lokala krökningsradier parallellt med sprickplanet som tillsammans med de vinkelräta krökningsradierna bidrar till det lokala kapillärtrycket. Ett passande antal platser (vilket ger en passande längd längs gränsytan) för att bestämma den lokala krökningen hos gränsytan väljs genom en adaptiv metod där antalet platser anpassas för bästa beskrivning av den lokala krökningen. Metoden är därmed adaptiv för den lokala krökningen av gränsytan, medan man med tidigare metoder måste välja samma längd (antal platser) längs gränsytan för beräkning av krökningsradien överallt i sprickplanet. ACF metoden implementerades i en invasion-perkolationsmodell (IP modell) och användes för simuleringar av tvåfasflöde som sedan jämfördes med tidigare publicerade experimentella data (Neuweiler m.fl., 2004) som beskriver dräneringsprocesser i två olika sprickor. Jämförelsen visade att ACF metoden kan återskapa de experimentella resultaten väl, både med avseende på direkt matchning av fluidernas distribution och fraktal dimension hos kluster av invaderande fas. Då krökningen av gränsytan parallellt med sprickplanet försummades i simuleringarna (standard invasion-perkolationsmodellering), blev resultatet kluster av invaderande fas som inte var tillräkligt kompakta för att matcha de experimentella observationerna, vilket visar vikten av att beakta krökningen av gränsytan parallellt med sprickplanet i dessa fall.

I artikel **III**, visar den jämförande studien att simuleringarna med den kontinuumbaserade modellen kan reproducera resultaten från IP modellen vid tvåfasflöde som domineras av kapillära krafter. Vidare kan den kontinuumbaserade modellen också simulera tvåfasflöden vid höga kapillärtal

eftersom viskösa tryckförluster beaktas. Dessutom kan den kontinuumbaserade modellen användas även då viss ömsesidig lösning eller omblandning av faserna sker (t.ex. superkritisk CO_2-saltlake) och för trefasflöde (t.ex. sprickor i omättade zonen med vatten, luft och organisk vätska). Den kontinuumbaserade modellen är dock beräkningsmässigt tungkörd och är därför begränsad till modellering med relativt få beräkningsceller. Om kontinuummodellen kan simulera gravitationsdrivet flöde vid höga Bondtal kvarstår att undersöka vidare. IP modellen, å andra sidan, är beräkningsmässigt tilltalande och möjliggör också att effekter av gränsytans krökning parallellt med sprickplanet kan beaktas (se artikel **II**). IP modeller kan också vidareutvecklas så att de omfattar en förstaordningens approximation av viskösa effekter (tryckförluster). Analyser med sådana vidareutvecklingar återfinns i aktuella publikationer (t.ex. Xu m.fl., 1998; Ferer m.fl., 2011). Det är också noterbart att vidare modellutveckling behövs för att förstå vissa komplexa fysikaliska fenomen som ibland observerats, så som fragmentering, pulsering och filmflöde vid gravitationsdestabiliserade flöden (t.ex. Meakin m.fl., 1992; Glass och Yarrington, 2003).

I artikel **IV**, undersöktes lösning av organisk vätska till grundvatten i en spricka med varierande apertur för två fastläggningsscenarier; droppar av organisk vätska som immobiliserats under gravitationsdrivet fingerflöde och pölansamlingar i en ”återvändsspricka” med stängd rand. I ett experiment med lösning av immobila droppar av organisk vätska i en vertikal analog glasspricka användes genomlysning med synligt ljus som mätmetod. Resultaten visade att den specifika gränsytan mellan organisk vätska och vatten approximativt minskar linjärt med mättnadsgraden av organisk vätska. En högupplöst mekanistisk numerisk modell utvecklades och kunde mycket väl reproducera den observerade lösningsprocessen i experimentet. Den numeriska modellen har använts för att simulera lösning av de immobila dropparna för olika grundvattenströmningshastigheter. Det simulerade förhållandet mellan Sherwoodtalet *Sh* (vilket representerar massöverföringstakten) och Peclettalet *Pe* (som representerar förhållandet mellan advektion och diffusion) kunde anpassas väl till en enkel potensfunktion ($Sh = 1.4Pe^{0.43}$). För att undersöka massöverföringsegenskaper hos pölansamlingar av organisk vätska i delvis stängda (”återvänds-”) sprickor användes numerisk modellering av fastläggning och lösning i vertikala sådana sprickor. När pölarna löstes upp ökade djupet av stillastående vatten ovanför dem linjärt med avtagandet i mättnadsgraden av organisk vätska. Det ökande djupet av stillastående vatten ovanför den organiska vätskan gjorde att vattenflödet ovanför blev mindre och mindre effektivt på att ta med sig den vattenlösta kemikalien, vilket tyder på att massöverföringstakten beror av djupet från flödande vatten till pölen, eller alternativt, den kvarvarande mängden organisk vätska i sprickan. Simuleringarna visade att det resulterande Sherwoodtalet var klart mindre än i fallet med immobila droppar av organisk vätska och att *Sh* kunde

anpassas väl till en potensfunktion som funktion av *Pe* och den kvarvarande andelen organisk vätska.

Slutligen föreslås några framtida forskningsteman som är relevanta för avhandlingsämnet. Dessa täcker både förståelse av småskaliga fysikaliska fenomen och storskalig (spricknätverks-) modellering. De inkluderar: (i) vidare förståelse av dynamiken i flerfasflöde under generella förhållanden där den sammantagna effekten av kapillära, viskösa och gravitationskrafter samt tröghet beaktas; (ii) hur sprickkorsningar och deras variation i rummet påverkar flerfasflöde och transport; (iii) påverkan av anisotropi i aperturfältet på flöde, massöverföring och ämnestransport; och (iv) prediktiv modellering av flerfasflöde och utmattning av föroreningskällor på fältskala i sprickiga medier.

References

Abriola, L. M., and S. A. Bradford (1998), Experimental Investigations of the Entrapment and Persistence of Organic Liquid Contaminants in the Subsurface Environment, *Environmental Health Perspectives*, *106*, 1083–1095.

Abriola, L. M., and G. F. Pinder (1985), A multiphase approach to the modeling of porous media contamination by organic compounds: 1. Equation development, *Water Resour. Res.*, 21(1), 11–18.

Amundsen, H., G. Wagner, U. Oxaal, P. Meakin, J. Feder, and T. Jøssang (1999), Slow two-phase flow in artificial fractures: Experiments and simulations, *Water Resour. Res.*, 35(9), 2619–2626, doi:10.1029/1999WR900147.

Aziz, K., and A. Settari (1979), *Petroleum reservoir simulation*, 476 pp., Applied Science Publishers, London.

Basu, N. B., A. D. Fure, and J. W. Jawitz (2008), Simplified contaminant source depletion models as analogs of multiphase simulators, *Journal of Contaminant Hydrology*, *97*(3-4), 87–99, doi:10.1016/j.jconhyd.2008.01.001.

Berkowitz, B. (2002), Characterizing flow and transport in fractured geological media: A review, *Advances in Water Resources*, *25*(8-12), 861–884, doi:10.1016/s0309-1708(02)00042-8.

Broadbent, S. R., and J. M. Hammersley (1957), Percolation processes, I, Crystals and mazes, *Proc. Cambridge Philos. Soc.*, 53, 629-641.

Brooks, R. H., and A. T. Corey (1964). Hydraulic properties of porous media. *Hydrology paper 3*, Colorado State University, Fort Collins, Colorado.

Brown, S. R. (1995), Simple mathematical model of a rough fracture, *J. Geophys. Res.*, 100(B4), 5941–5952, doi:10.1029/94JB03262.

Brown, S. R., R. L. Kranz, and B. P. Bonner (1986), Correlation between the surfaces of natural rock joints, *Geophys. Res. Lett.*, *13*(13), 1430–1433, doi:10.1029/GL013i013p01430.

Chambon, J. C., M. M. Broholm, P. J. Binning, and P. L. Bjerg (2010), Modeling multi-component transport and enhanced anaerobic dechlorination processes in a single fracture-clay matrix system., *Journal of Contaminant Hydrology*, *112*(1-4), 77–90, doi: doi:10.1016/j.jconhyd.2009.10.008.

Chaouche, M., N. Rakotomalala, D. Salin, B. Xu, and Y. C. Yortsos (1994), Invasion percolation in a hydrostatic or permeability gradient: Experiments and simulations, *Physical Review E*, *49*(5), 4133–4139, doi:10.1103/PhysRevE.49.4133.

Chen, C.-Y., and R. N. Horne (2006), Two-phase flow in rough-walled fractures: Experiments and a flow structure model, *Water Resour. Res.*, *42*(3), W03430, doi:10.1029/2004WR003837.

Detwiler, R. L., S. E. Pringle, and R. J. Glass (1999), Measurement of fracture aperture fields using transmitted light: An evaluation of measurement errors and their influence on simulations of flow and transport through a single fracture, *Water Resour. Res.*, *35*(9), 2605–2617, doi:10.1029/1999wr900164.

Detwiler, R. L., H. Rajaram, and R. J. Glass (2001), Nonaqueous-phase-liquid dissolution in variable-aperture fractures: Development of a depth-averaged computational model with comparison to a physical experiment, *Water Resour. Res.*, *37*(12), 3115–3129, doi:10.1029/2000wr000161.

Detwiler, R. L., H. Rajaram, and R. J. Glass (2005), Satiated relative permeability of variable-aperture fractures, *Physical Review E*, *71*, 31114, doi:10.1103/PhysRevE.71.031114.

Detwiler, R. L., H. Rajaram, and R. J. Glass (2009), Interphase mass transfer in variable aperture fractures: Controlling parameters and proposed constitutive relationships, *Water Resour. Res.*, *45*(8), W08436, doi:10.1029/2008wr007009.

Dickson, S. E., and N. R. Thomson (2003), Dissolution of entrapped DNAPLs in variable aperture fractures: Experimental data and empirical model, *Environmental Science & Technology*, *37*(18), 4128–4137, doi:10.1021/es026275r.

Dijk, P., B. Berkowitz, and P. Bendel (1999), Investigation of flow in water-saturated rock fractures using nuclear magnetic resonance imaging (NMRI), *Water Resour. Res.*, *35*(2), 347–360, doi:10.1029/1998WR900044.

Falta, R.W. (2005), Dissolved chemical discharge from fractured clay aquitards contaminated by DNAPLs. In: Faybishenko, B., Witherspoon, P.A., Gale, J. (Eds.), *Dynamics of Fluids in Fractured Rocks*. Geophysical Monograph, 162, pp. 165–174, American Geophysical Union, Washington, D.C.

Falta, R.W., K. Pruess, S. Finsterle and A. Battistelli (1995), T2VOC User's Guide, *Report LBL-36400, UC-400*, Lawrence Berkeley National Laboratory, Berkeley, Calif.

Ferer, M., G. S. Bromhal, and D. H. Smith (2005), Two-phase flow in porous media: Crossover from capillary fingering to compact invasion for drainage, *Physical Review E*, *71*(2), 26303, doi:10.1103/PhysRevE.71.026303.

Ferer, M., D. Crandall, G. Ahmadi, and D. H. Smith (2011), Two-phase flow in a rough fracture: Experiment and modeling, *Physical Review E*, *84*(1), 16316, doi:10.1103/PhysRevE.84.016316.

Ferer, M., C. Ji, G. S. Bromhal, J. Cook, G. Ahmadi, and D. H. Smith (2004), Crossover from capillary fingering to viscous fingering for immiscible unstable flow: Experiment and modeling, *Physical Review E*, *70*(1), 16303, doi/10.1103/PhysRevE.70.016303.

Frette, O. I., K. J. Måløy, J. Schmittbuhl, and A. Hansen (1997), Immiscible displacement of viscosity-matched fluids in two-dimensional porous media, *Physical Review E*, *55*(3), 2969–2975, doi:10.1103/PhysRevE.55.2969.

Gale, J.E. (1987), Comparison of coupled fracture deformation and fluid flow models with direct measurements of fracture pore structure and stress-flow properties. In: *Proceedings of the 28th U.S. Symposium on Rock Mechanics*, Brookfield, Vt., pp. 1213–1222.

Glass, R. J. (1993), Modeling gravity-driven fingering in rough-walled fractures using modified percolation theory, in *High Level Radioactive Waste Management: Proceedings of the Fourth Annual International Conference*, pp. 2042–2053, Am. Nucl. Soc., LaGrange Park, Ill.

Glass, R. J., M. J. Nicholl, and L. Yarrington (1998), A modified invasion percolation model for low-capillary number immiscible displacements in horizontal rough-walled fractures: Influence of local in-plane curvature, *Water Resour. Res.*, *34*(12), 3215-3234. (Correction, *Water Resour. Res., 36*(7), 1991, doi:10.1029/2000WR900060, 2000.)

Glass, R.J., H. Rajaram, and R.L. Detwiler (2003), Immiscible displacements in rough-walled fractures: Competition between roughening by random aperture

variations and smoothing by in-plane curvature, *Physical Review E*, 68, 061110, doi:10.1103/PhysRevE.68.061110.

Glass, R. J., H. Rajaram, M. J. Nicholl, and R. L. Detwiler (2001), The interaction of two fluid phases in fractured media, *Current Opinion in Colloid & Interface Science*, *6*(3), 223–235, doi:10.1016/s1359-0294(01)00086-3.

Glass, R. J., and L. Yarrington (2003), Mechanistic modeling of fingering, nonmonotonicity, fragmentation, and pulsation within gravity/buoyant destabilized two-phase/unsaturated flow, *Water Resour. Res.*, 39(3), 1058, doi:10.1029/2002WR001542.

Hakami, E. and E. Larsson (1996), Aperture measurements and flow experiments on a single natural fracture, *Int. J. Rock Mech. Min. Sci. & Geomech. Abstr. 33* (4), 395–404, doi:10.1016/0148-9062(95)00070-4.

Hughes, R. G. and M. J. Blunt (2001), Network modeling of multiphase flow in fractures, *Adv. Water Resour., 24*, 409–421, doi:10.1016/s0309-1708(00)00064-6.

Ji, S.-H., I. W. Yeo, K.-K. Lee, and R. J. Glass (2003), Influence of ambient groundwater flow on DNAPL migration in a fracture network: Experiments and simulations, *Geophys. Res. Lett.*, *30*(10), 1504, doi:10.1029/2003gl017064.

Karpyn, Z. T., A. S. Grader, and P. M. Halleck (2007), Visualization of fluid occupancy in a rough fracture using micro-tomography, *Journal of Colloid and Interface Science*, *307*(1), 181-187, doi:10.1016/j.jcis.2006.10.082.

Karpyn, Z. T., and M. Piri (2007), Prediction of fluid occupancy in fractures using network modeling and x-ray microtomography. I: Data conditioning and model description, *Physical Review E*, *76*, 16315, doi:10.1103/PhysRevE.76.016315.

Keller, A. (1998), High resolution, non-destructive measurement and characterization of fracture apertures, *International Journal of Rock Mechanics and Mining Sciences*, *35*(8), 1037–1050, doi:10.1016/s0148-9062(98)00164-8.

Keller, A. A., M. J. Blunt and P. V. Roberts (2000), Behavior of dense non-aqueous phase liquids in fractured porous media under two-phase flow conditions, *Transport in Porous Media*, 38: 189-203, doi:10.1023/A:1006619402305.

Keller, A. A., P. V. Roberts, and M. J. Blunt (1999), Effect of fracture aperture variations on the dispersion of contaminants, *Water Resour. Res.*, *35*(1), 55–63, doi:10.1029/1998wr900041.

Keller, A. A., P. V. Roberts, and P. K. Kitanidis (1995), Prediction of single phase transport parameters in a variable aperture fracture, *Geophys. Res. Lett.*, *22*(11), 1425–1428, doi:10.1029/95gl01497.

Khachikian, C., and T. C. Harmon (2000), Nonaqueous phase liquid dissolution in porous media: Current state of knowledge and research needs, *Transport in Porous Media*, *38*(1), 3–28, doi:10.1023/A:1006667318234.

Kueper, B.H., G.P. Wealthall, J.W.N., Smith, S.A. Leharne and D.N. Lerner (2003), An illustrated handbook of DNAPL transport and fate in the subsurface. *UK Environment Agency R&D Publication 133*. ISBN 1844320669.

Lapcevic, P. A., K. S. Novakowski, and E. A. Sudicky (1999), The interpretation of a tracer experiment conducted in a single fracture under conditions of natural groundwater flow, *Water Resour. Res.*, *35*(8), 2301–2312, doi:10.1029/1999WR900143.

Lee, J., J. M. Kang, and J. Choe (2003), Experimental analysis on the effects of variable apertures on tracer transport, *Water Resour. Res.*, *39*(1), 1015, doi:10.1029/2001wr001246.

Liechti, K. M., S. T. Schnapp, and J. G. Swadener (1997), Contact angle and contact mechanics of a glass/epoxy interface, *International Journal of Fracture*, *86*, 361–374, doi:10.1023/A:1007472628431.

Lipson, D. S., B. H. Kueper, and M. J. Gefell (2005), Matrix Diffusion-Derived Plume Attenuation in Fractured Bedrock, *Ground Water*, *43*(1), 30–39, doi:10.1111/j.1745-6584.2005.tb02283.x.

Loggia, D., Z. Bo, X. Luo, and G. Vasseur (2009), Experimental study of upward oil migration in a fracture, *Transport in Porous Media*, 80(1), 1-16, doi : 10.1007/s11242-009-9340-2.

Mackay, D. M., and J. A. Cherry (1989), Groundwater contamination: pump-and-treat remediation, *Environmental Science & Technology*, *23*(6), 630-636, doi:10.1021/es00064a001.

Meakin, P., A. Birovljev, V. Frette, J. Feder, and T. Jøssang (1992), Gradient stabilized and destabilized invasion percolation, *Physica A*, 191, 227–239, doi:10.1016/0378-4371(92)90532-U.

Meakin P., G. Wagner, A. Vedvik, H. Amundsen, J. Feder, and T. Jøssang (2000), Invasion percolation and secondary migration: experiments and simulations, *Mar. Petrol. Geol.,* 17, 777–795, doi:10.1016/s0264-8172(99)00069-0.

Mercer, J. W., and R. M. Cohen (1990), A review of immiscible fluids in the subsurface: Properties, models, characterization and remediation, *Journal of Contaminant Hydrology*, *6*(2), 107–163, doi:10.1016/0169-7722(90)90043-g.

Murphy, J. R., and N. R. Thomson (1993), Two-phase flow in a variable aperture fracture, *Water Resour. Res.*, 29(10), 3453–3476, doi:10.1029/93WR01285.

Neuweiler, I., I. Sorensen, and W. Kinzelbach (2004), Experimental and theoretical investigations of drainage in horizontal rough-walled fractures with different correlation structures, *Adv. Water Resour.*, 27(12), 1217-1231, doi:10.1016/j.advwatres.2004.07.005.

Neuman, S. P. (2005), Trends, prospects and challenges in quantifying flow and transport through fractured rocks, *Hydrogeology Journal*, *13*(1), 124–147, doi:10.1007/s10040-004-0397-2.

Nicholl, M.J., and R.J., Glass (2005), Infiltration into an analog fracture: Experimental observations of gravity-driven fingering, *Vadose Zone J.*, 4, 1123–1151, doi:10.2136/vzj2004.0110.

Novakowski, K. S., P. A. Lapcevic, J. Voralek, and G. Bickerton (1995), Preliminary interpretation of tracer experiments conducted in a discrete rock fracture under conditions of natural flow, *Geophys. Res. Lett.*, *22*(11), 1417–1420, doi:10.1029/95gl00569.

Nowamooz, A., G. Radilla, and M. Fourar (2009), Non-Darcian two-phase flow in a transparent replica of a rough-walled rock fracture, *Water Resour. Res.*, 45, W07406, doi:10.1029/2008WR007315.

NRC (1996), *Rock fractures and fluid flow: Contemporary understanding and Applications*, 551 pp., National Academy Press, Washington, D.C.

NRC (2005), *Contaminants in the Subsurface: Source zone assessment and remediation*, 344 pp., National Academy Press, Washington, D.C.

Oostrom, M., J. H. Dane, and T. W. Wietsma (2007), A review of multidimensional, multifluid, intermediate-scale experiments: Flow behavior, saturation imaging, and tracer detection and quantification, *Vadose Zone Journal*, *6*(3), 610, doi:10.2136/vzj2006.0178.

Oostrom, M., J. H. Dane, and T. W. Wietsma (2006), A review of multidimensional, multifluid, intermediate-scale experiments: Nonaqueous phase liquid dissolu-

tion and enhanced remediation, *Vadose Zone J.*, *5*(2), 570–598, doi:10.2136/vzj2005.0125.

Oron, A. P., and B. Berkowitz (1998), Flow in rock fractures: The local cubic law assumption reexamined, *Water Resour. Res.*, *34*(11), 2811–2825, doi:10.1029/98wr02285.

Parker, B. L., D. B. McWhorter, and J. A. Cherry (1997), Diffusive loss of non-aqueous phase organic solvents from idealized fracture networks in geologic media, *Ground Water*, *35*(6), 1077–1088, doi:10.1111/j.1745-6584.1997.tb00180.x.

Parker, J. C., and E. Park (2004), Modeling field-scale dense nonaqueous phase liquid dissolution kinetics in heterogeneous aquifers, *Water Resour. Res.*, *40*(5), W05109, doi:10.1029/2003wr002807.

Persoff, P., and K. Pruess (1995), Two-phase flow visualization and relative permeability measurement in natural rough-walled rock fractures, *Water Resour. Res.*, *31*(5), 1175-1186, doi:10.1029/95wr00171.

Petchsingto, T., and Z. Karpyn (2010), Simulation of fluid percolation in a rough-walled rock fracture, *Hydrogeology Journal*, *18*(7), 1583-1589, doi:10.1007/s10040-010-0632-y.

Piri, M., and Z. T. Karpyn (2007), Prediction of fluid occupancy in fractures using network modeling and x-ray microtomography. II: Results, *Physical Review E*, *76*, 16316, doi:10.1103/PhysRevE.76.016316.

Pruess, K., C. Oldenburg, and G. Moridis (1999), TOUGH2 User's Guide, Version 2.0, *Report LBNL-43134*, Lawrence Berkeley National Laboratory, Berkeley, California.

Pruess, K., and Y. W. Tsang (1990), On two-phase relative permeability and capillary pressure of rough-walled rock fractures, *Water Resour. Res.*, 26(9), 1915–1926, doi:10.1029/WR026i009p01915.

Pyrak-Nolte, L. J., D. Helgeson, G. M. Haley and J. W. Morris (1992), *Immiscible fluid flow in a fracture.* In: Tillerson J. R. and Wawersik W. R., Editors*, Rock mechanics, Proceedings of the 33rd US Symposium*, Rotterdam, Netherlands: A.A. Balkema, 571–578, 1992.

Rasmuson, A., and I. Neretnieks (1986), Radionuclide transport in fast channels in crystalline rock, *Water Resour. Res.*, 22(8), 1247–1256, doi: 10.1029/WR022i008p01247.

Raven, K. G., and J. E. Gale (1985), Water flow in a natural rock fracture as a function of stress and sample size, *International Journal of Rock Mechanics and Mining Sciences & Geomechanics Abstracts*, *22*(4), 251–261, doi:10.1016/0148-9062(85)92952-3.

Raven, K. G., K. S. Novakowski, and P. A. Lapcevic (1988), Interpretation of field tracer tests of a single fracture using a transient solute storage model, *Water Resour. Res.*, *24*(12), 2019–2032, doi:10.1029/WR024i012p02019.

Reitsma, S., and B. H. Kueper (1994), Laboratory measurement of capillary pressure-saturation relationships in a rock fracture, *Water Resour. Res.*, 30(4), 865-878, doi:10.1029/93wr03451.

Reynolds, D. A., and B. H. Kueper (2003), Effective constitutive properties for dense nonaqueous phase liquid (DNAPL) migration in large fracture networks: A computational study, *Water Resour. Res.*, *39*(9), 1254, doi:10.1029/2002wr001684.

Sahimi, M. (2011), *Flow and transport in porous media and fractured rock*, 718 pp., Wiley-VCH Verlag, Weinheim, Germany.

Schaefer, C. E., A. V. Callaghan, J. D. King, and J. E. McCray (2009), Dense nonaqueous phase liquid architecture and dissolution in discretely fractured

sandstone blocks, *Environmental Science & Technology*, *43*(6), 1877–83, doi:10.1021/es8011172.

Schaefer, C. E., R. M. Towne, S. Vainberg, J. E. McCray, and R. J. Steffan (2010), Bioaugmentation for treatment of dense non-aqueous phase liquid in fractured sandstone blocks, *Environmental Science & Technology*, *44*(13), 4958-64, doi:10.1021/es1002428.

Su, G.W., J. T. Geller, J. R. Hunt, and K. Pruess (2004): Small-scale features of gravity-driven flow in unsaturated fractures. *Vadose Zone J.* 3, 592–601, doi:10.2113/3.2.592.

Su G. W. and I. Javandel (2004), DNAPL invasion into a partially saturated dead-end fracture, *Report LBNL-55535*, Lawrence Berkeley National Laboratory, Berkeley, California.

Tunnicliffe, B. S., and N. R. Thomson (2004), Mass removal of chlorinated ethenes from rough-walled fractures using permanganate, *Journal of Contaminant Hydrology*, *75*(1-2), 91–114, doi:10.1016/j.jconhyd.2004.04.006.

VanderKwaak, J. E., and E. A. Sudicky (1996), Dissolution of non-aqueous-phase liquids and aqueous-phase contaminant transport in discretely-fractured porous media, *Journal of Contaminant Hydrology*, *23*(1-2), 45–68, doi:10.1016/0169-7722(95)00087-9.

Van Genuchten, M. T. (1980), A closed-form equation for predicting the hydraulic conductivity of unsaturated soils, *Soil Sci. Soc. Am. J.*, 44, 892-898, doi: 10.2136/sssaj1980.03615995004400050002x.

Werner, P. G., and M. F. Helmke (2003), Chemical oxidation of tetrachloroethene in a fractured saprolite/bedrock aquifer, *Remediation Journal*, *14*(1), 95-107, doi:10.1002/rem.10097.

Wilkinson, D., and J. F. Willemsen (1983), Invasion percolation: A new form of percolation theory, *J. Phys. A Math. Gen*., 16, 3365– 3376.

Xu, B., Y. C. Yortsos, and D. Salin (1998), Invasion percolation with viscous forces, *Phys. Rev. E*, 57(1), 739–751, doi:10.1103/PhysRevE.57.739.

Yeo, I. W., S.-H. Ji, and K.-K. Lee (2003), Density-surfactant-motivated removal of DNAPL trapped in dead-end fractures, *Geophys. Res. Lett.*, *30*(9), 1471, doi:10.1029/2003gl017186.

Acta Universitatis Upsaliensis

Digital Comprehensive Summaries of Uppsala Dissertations from the Faculty of Science and Technology 994

Editor: The Dean of the Faculty of Science and Technology

A doctoral dissertation from the Faculty of Science and Technology, Uppsala University, is usually a summary of a number of papers. A few copies of the complete dissertation are kept at major Swedish research libraries, while the summary alone is distributed internationally through the series Digital Comprehensive Summaries of Uppsala Dissertations from the Faculty of Science and Technology.

Distribution: publications.uu.se
urn:nbn:se:uu:diva-183720

ACTA
UNIVERSITATIS
UPSALIENSIS
UPPSALA
2012